Triple iron isotope constraints on the role of ocean iron sinks in early atmospheric oxygenation

Andy W Heard, Nicolas Dauphas, Romain Guilbaud, Olivier J Rouxel, Ian B Butler, Nicole X Nie, Andrey Bekker

Resolving the Role of Ocean Iron Sinks in Early Atmospheric Oxygenation

Andy W. Heard[1*], Nicolas Dauphas[1], Romain Guilbaud[2], Olivier J. Rouxel[3], Ian B. Butler[4], Nicole X. Nie[1], Andrey Bekker[5]

[1]Origins Laboratory, Department of the Geophysical Sciences and Enrico Fermi Institute, The University of Chicago, 5734 South Ellis Avenue, Chicago, IL 60637, USA.
[2]Géosciences Environnement Toulouse, CNRS, UMR5563, 14 Avenue Edouard Belin, 31400 Toulouse, France.
[3]IFREMER, Plouzané 56470, France.
[4]School of Geosciences, University of Edinburgh, Grant Institute, Edinburgh EH9 3JW, UK.
[5]Department of Earth and Planetary Sciences, University of California, Riverside, CA 92521, USA.
*e-mail: andyheard@uchicago.edu

Submitted to Science

2259 words, 3 figures

Abstract (113 words)

The role that iron played in the oxygenation of Earth's surface is equivocal. Iron could have consumed O_2 during Fe^{2+} oxidation or released O_2 during pyrite burial fueled by volcanic SO_2. Through high-precision Fe isotopic measurements of Archean-Paleoproterozoic sediments and laboratory grown pyrites, we show that the triple-Fe-isotopic composition of Neoarchean-Paleoproterozoic pyrites requires both extensive marine iron oxidation and sulfide-limited pyritization. Using an isotopic fractionation model informed by these new constraints, we resolve the relative sizes of marine oxide and pyrite sinks for Neoarchean marine iron. We show that pyrite burial could have resulted in O_2 export exceeding local Fe^{2+} oxidation sinks, thus contributing to early episodes of oxygenation of the Archean atmosphere.

Main Text

Irreversible changes of oxic and euxinic sedimentary iron sinks during the Archean and Paleoproterozoic were intimately linked with the oxygenation of Earth's atmosphere during the Great Oxygenation Event (GOE), beginning ca. 2.43 Ga (*1*, *2*). Early episodes of oxygenation coincided with enhanced burial of iron sulfide (pyrite) in sediments (*3*–*5*). This limb of the pre-GOE Fe cycle may have directly contributed to early atmospheric oxygenation, as enhanced volcanic SO_2 fluxes accompanying Neoarchean continental emergence may have contributed to net burial of reducing power in sedimentary pyrite, following microbial sulfate reduction (*6*–*8*). Early environmental oxidation should have been buffered by reduced species in the ocean and atmosphere, principally Fe^{2+}. Therefore, the marine iron cycle potentially played roles on both sides of Earth's early oxygenation. Major shifts in Fe isotopic records occur across the GOE (*9*, *10*) (Fig. 1A), and reflect evolution of the Fe, S, and O cycles through the Archean and Paleoproterozoic (*11*). Interpretation of the Fe isotopic composition of pre-GOE pyrites, which can be depleted in $^{56}Fe/^{54}Fe$ ratio by as much as -3.5‰, a degree unseen in the post-GOE rock record (*9*), is however not straightforward. The reason is that these pyrite Fe isotopic compositions could be controlled by (*i*) the size of oxidizing iron sinks that removed isotopically heavy Fe^{3+} oxides, leaving a pool of isotopically light dissolved Fe^{2+} from which pyrite could have formed (*9*, *10*); (*ii*) microbial dissimilatory Fe^{3+} reduction (DIR) that preferentially releases an isotopically light Fe^{2+} pool (*12*, *13*); and (*iii*) kinetic isotope effects (KIEs) accompanying partial pyrite precipitation, which can produce isotopically light pyrite (*14*, *15*). The relative importance of these processes remains heavily debated (*9*–*18*), and this uncertainty has hindered quantitative interpretation of the ancient iron cycle, exemplified by the fact that $\delta^{56}Fe$ records have not yet constrained the degree to which Fe sedimentation on highly productive continental margins was a net sink or source for early O_2 (*8*).

Here, we report triple-Fe-isotopic ratio measurements that allow us to remove ambiguities in previous interpretations of the pre-GOE iron cycle. This approach relies on our discovery that the main isotopic fractionation processes implicated in the formation of pre-GOE pyrites follow distinct isotopic mass fractionation laws (MFLs), which describe how different isotopic ratios of the same element covary (*19*, *20*). To resolve MFLs, measurement of Fe isotopic ratios must be of a higher precision than has previously been achieved in analysis of ancient sediments. A similar approach has been used once in igneous geochemistry to demonstrate that Fe isotopic variations

in magmatic olivine followed a kinetic MFL for diffusive transport (*21*). For a given MFL, the ratio of $^{56}Fe/^{54}Fe$ to that of $^{57}Fe/^{54}Fe$ defines the slope

$$\theta^{56/57} = \delta'^{56}Fe/\delta'^{57}Fe \quad \text{(Eq. 1)}$$

where $\delta'^{x}Fe = 1{,}000 \ln[(^{x}Fe/^{54}Fe)_{sample}/(^{x}Fe/^{54}Fe)_{IRMM\text{-}014}]$ (IRMM-014 is a standard reference material consistent with bulk planetary composition) (*20*, *22*). Isotopic trends following an array of MFLs are by definition mass-dependent; but they manifest as apparent departures, $\epsilon'^{56}Fe$, from an arbitrary reference MFL (*20*, *23*, *24*), which we choose here to be the high-temperature equilibrium limit law with $\theta^{56/57}$=0.678, where

$$\epsilon'^{56}Fe = [\delta'^{56}Fe - 0.678 \times \delta'^{57}Fe] \times 10 \quad \text{(Eq. 2)}$$

In $\epsilon'^{56}Fe$ *vs.* $\delta'^{57}Fe$ space, MFLs form straight lines whose slopes can be related to $\theta^{56/57}$ through

$$\epsilon'^{56}Fe = 10 \times [\theta^{56/57} - 0.678] \times \delta'^{57}Fe \quad \text{(Eq. 3)}$$

In order to establish the values of $\theta^{56/57}$ corresponding to the two endmember hypotheses that have been put forward to explain the $\delta'^{56}Fe$ pyrite record (*9*, *10*, *14*), we measured:

(*i*) A suite of iron formation (IF) samples that show a large range in $\delta'^{56}Fe$ values, including Mn-rich IFs from the Hotazel Formation in the Griqualand West sub-basin, South Africa, dated at ca. 2.43 Ga (*2*), that were presumably precipitated from an iron pool that had experienced extensive oxidative iron removal, resulting in IFs characterized by anomalously low $\delta'^{56}Fe$ values (*25*).

(*ii*) Experimental products of pyrite synthesis via the FeS-H_2S pathway, which produced pyrite with $\delta'^{56}Fe$ values as low as -2.4‰ relative to the initial iron pool (Figs. 1B, S2) (*24*). In these experiments, we precipitated pyrite in anoxic conditions from an FeS precursor (*24*) following a protocol established by Guilbaud et al. (*14*, *24*).

The IFs define a slope of $\theta^{56/57}_{ox}$=0.6776±0.0004 for the oxidizing ($_{ox}$) iron sink (here and elsewhere, the error bars are 95% confidence intervals), which agrees with theoretical expectations for equilibrium isotope exchange that dominates during iron oxidation (*20*, *22*), while the pyrite-precipitation experiments gave $\theta^{56/57}_{KIE}$=0.6743±0.0006 (Fig. 1B). Triple-Fe-isotopic slopes for the two endmember scenarios are clearly distinct, allowing us to use these slopes to address what caused Fe isotopic variations in natural pyrites before the GOE.

We analyzed a suite of pre-GOE Neoarchean-Paleoproterozoic pyrites with highly depleted $\delta'^{56}Fe$ values (as low as -3.1 ‰) and a few bulk black shales from the same formations. The pyrite and shales fall in an intermediate space in the triple Fe isotope diagram between the endmember

MFLs for Fe^{2+} oxidation and pyrite precipitation. A linear regression through these data would have a slope of 0.6761±0.0006, but we do not interpret the apparent linear trend as an MFL, because the pyrite and shale array is composed of samples from several distinct formation and each sample requires contributions from more than one fractionation process (with distinct MFLs) and therefore has no mechanistic significance. More likely, pre-GOE pyrite $\delta'^{56}Fe$ values record a two-step process; partial marine Fe^{2+} oxidation during non-steady-state upwelling of Fe^{2+}-rich deep waters (*9*), and subsequent KIEs during partial, sulfide-limited pyrite formation from the remaining Fe^{2+} reservoir (*14*, *15*, *26*). In this model, oxic and pyrite sinks sequestered iron upwelling from deep ocean basins lacking a discrete redoxcline, towards black shale depositional settings (Fig. S7)(*10*, *24*, *27*) .

For any isotopically light pyrite sample, we can estimate contributions to the $\delta'^{56}Fe$ value from prior iron-oxidation, and the KIE during pyritization in the porewater iron reservoir. We calculate contributions of Fe-oxidation to $\delta'^{56}Fe$ values of the water mass ($\delta'^{56}Fe_w$) from intercepts with the oxidation MFL, and determined the Fe isotopic fractionation imparted by pyritization by taking the difference in $\delta'^{56}Fe$ values between those of pyrite and $\delta'^{56}Fe_w$ (Figs. 2A, S5) (*24*). An underlying assumption in this calculation is that sedimentary pyrite formed from a pool of dissolved Fe^{2+} that sampled the marine Fe^{2+} reservoir (*9*), although the nodular nature of the pyrites indicates that they formed in sediments through diagenesis. A major source of iron in porewaters would presumably have been downward diffusion of overlying Fe^{2+}-rich seawater into the sediment (*9*). We cannot exclude however that some porewater Fe^{2+} was produced by DIR (*12*, *13*). This is an uncertainty in our model. However, the role of partial (isotopically fractionating) DIR in the host shales of these pyrites is not supported by Fe isotopic compositions of bulk shale material, which lacks the complimentary heavy isotopic signature that would be expected of a DIR residue (*26*). Additionally, coupled Fe and C isotope analyses of Archean sediments suggests that DIR occurred in a closed system with respect to isotopes, with diagenetic carbonate minerals taking on the composition of their precursor oxides (*28*, *29*). While we cannot rule out the additional influence of DIR in the origin of pre-GOE pyrite Fe isotopic signatures, we anticipate that any uncertainty it introduces would be transferred to interpretations of $\delta'^{56}Fe_w$ values, and not the departures of triple Fe isotopic values from the Fe^{2+} oxidation MFL. The reason for this is that experiments to date suggest that the isotopic fractionation during DIR is an expression of the

equilibration of Fe^{2+} and Fe^{3+} after the reduction step (*30*), and therefore we expect it would fall into the same class of Fe redox equilibrium processes that define the Fe^{2+} oxidation MFL.

The fraction of Fe^{3+}-(oxyhydr)oxide removed to give the $\delta'^{56}Fe_w$ value on the intercept (F_{ox} = Fe in oxide sink/total Fe), and the fraction of pyrite removed from that remaining Fe^{2+} pool (f_{py} = Fe in pyrite/Fe remaining after Fe removal in the oxide sink), are both calculated assuming Rayleigh fractionation conditions (Figs. 2, S5; Table S4) (*24*) following upwelling of Fe^{2+}-rich deep water across the redoxcline (Fig. 2B). The fractional pyrite sink F_{py} for iron in the whole depositional system is $F_{py} = f_{py} \times (1 - F_{ox})$. Values of F_{ox} increase heading to more negative $\delta'^{57}Fe$ and $\epsilon'^{56}Fe$ values, whereas f_{py} decrease away from the oxidation MFL, reflecting preservation of a larger KIE at lower degrees of pyritization (Fig. 2B). F_{py} decreases strongly with decreasing $\delta'^{57}Fe$, due to the combined effects of decreasing f_{py} and increasing F_{ox} in this direction (Fig.S5). Contours of F_{ox}/F_{py} are sub-horizontal, making $\epsilon'^{56}Fe$ measurements highly diagnostic of the relative size of the oxic and pyritic sinks (Fig. 2C).

To fully propagate the effect of uncertainties in sample measurements; $\theta^{56/57}$ values for the endmember processes; and model fractionation factors; on uncertainties in F_{ox}, f_{py}, and F_{py}, we also used a Monte-Carlo simulation (Fig. 3). Estimates for F_{py} are 10 – 80 % of the upwelled iron pool (within 95 % C.I.) among the low $\delta'^{56}Fe$ pyrites we studied. With initial pre-GOE deep-water [Fe^{2+}] concentrations ~50 µM (*1*), the pyrite sink could have removed 5-40 µM of dissolved iron. This requires ~10-80 µM of seawater-dissolved sulfate to be microbially reduced to sulfide, ~350 to 1,400 times lower than the modern seawater sulfate concentration of 28 mM, and within recent estimates for Archean seawater sulfate based on S isotopic modelling (*31, 32*). For the ~2.65 Ga Jeerinah and Lokammona formations, we infer that as little as 10 % of iron upwelled onto the shelf was deposited as pyrite in euxinic sediments (Figs 2B, 3, S6) (*24*).

When volcanic SO_2 is the primary sulfur source, burial of reduced S in pyrite has a net oxidative effect on Earth's surface (*6*–*8*). For example, the reaction $2SO_2 + H_2O + Fe^{2+} \rightarrow FeS_2 + 2H^+ + 2.5O_2$, describing the net effect of SO_2 photolysis and hydrolysis, cyanobacterial photosynthesis, microbial sulfate reduction, and pyrite precipitation, indicates that pyrite burial can directly promote the net export of O_2 to the atmosphere-ocean system (*8*). The reaction is a maximum estimate for O_2 export during pyrite burial, because a more reduced original sulfur source would weaken the net oxidative effect of pyrite burial; and other types of primary productivity could have contributed organic matter for sulfate reduction, but only cyanobacterial

activity could have produced O_2. A more realistic estimate of volcanic H_2S/SO_2 emission ratios ~1 (*7*) would instead imply a net O_2 yield of 1 mole per mole of pyrite buried.

To oxygenate the atmosphere via pyrite burial, the produced O_2 would also need to overcome O_2 buffers in the ocean, primarily the upwelled Fe^{2+} flux. O_2-driven Fe^{2+} oxidation consumes 0.25 moles of O_2 per mole of Fe^{3+} buried, so net O_2 sources and sinks will be balance when $F_{ox}/F_{py} = 4$ (10) for volcanic H_2S/SO_2 emission ratios = 1 (0). Lower (higher) F_{ox}/F_{py} ratios indicate that Fe sedimentation in these settings was a net source (sink) of O_2 to the ocean-atmosphere system. Triple-Fe-isotopic systematics are strongly diagnostic for F_{ox}/F_{py} ratios, particularly at high values of this ratio where the switch from net O_2 source to sink behavior occurs (Fig. 2C). Pre-GOE pyrite data all fall at $F_{ox}/F_{py} < 4$ contour, and the $F_{ox}/F_{py} < 10$ falls outside of the error bar on individual pyrite $\epsilon'^{56}Fe$ values, so we can robustly rule out net O_2 sink-like behavior in the case where SO_2 dominated Neoarchean volcanic emissions. Even with conservative H_2S/SO_2 ratios (*7*) our data would imply a net O_2 source existed in Neoarchean pyrite-forming environments, particularly after 2.52 Ga (Figs 2C, 3). Average results from Monte Carlo simulations imply that the majority (>70 %) of O_2 liberated during pyrite burial could have remained to be released to the ocean-atmosphere system after exhausting local Fe^{2+} oxidation sinks. Despite the large net O_2 yield implied by all the formations we studied, evidence for whiffs of O_2 at ca. 2.65 Ga is weak (*33*) compared to the ca. 2.5 Ga event recorded by the Mt McRae Shale (*4*, *34*). The ca. 2.65 Ga Jeerinah and Lokammona formations indicate higher relative F_{ox}/F_{py} ratios and lower net O_2 yields (Figs 2C, 3). This raises the possibility that the real (non-idealized) threshold value for net O_2 release during Fe upwelling and pyrite burial lies on a F_{ox}/F_{py} contour separating 2.65 Ga pyrites (represented by the four most isotopically depleted pyrite samples in this study) from younger, higher $\delta'^{56}Fe$ samples (Fig. 2C).

The triple-Fe-isotope proxy provides a new and greater insight to the iron cycle in the early Earth's oceans. Before the GOE, large and probably fluctuating continental and hydrothermal iron fluxes to the oceans (*27*) were removed to two sedimentary sinks (Fig. S7)(*24*). The major sink was Fe^{3+}-(oxyhydr)oxides that were deposited from upwelling water masses in the oceans that lacked a discrete redoxcline and allowed protracted partial iron oxidation (*9*, *10*). The secondary iron sink was on highly productive continental margins, where deposition of pyrite-rich sediments was generally sulfate-limited. Small relative changes in iron removal to these oxide and sulfide sinks potentially led to perturbations in the net O_2 supply to the atmosphere, and surface ocean

oxygenation (*6*, *7*), triggering short-lived, episodic whiffs of O_2 (*8*). The loss of extremely negative $\delta^{56}Fe$ values in sedimentary pyrite formed after the GOE shows how this transition irreversibly changed the early Earth's iron cycle by decreasing iron flux to the oceans following the emergence of oxidative continental weathering; developing a discrete water-column redoxcline; and increasing supply of sulfate from the continents, which resulted in a shift in the major iron sink to extensively developed euxinic settings.

References and Notes

1. 1. H. D. Holland, *The Chemical Evolution of the Atmosphere and Oceans* (Princeton University Press, 1984).

2. A. P. Gumsley, K. R. Chamberlain, W. Bleeker, U. Söderlund, M. O. de Kock, E. R. Larsson, A. Bekker, Timing and tempo of the Great Oxidation Event. *Proc. Natl. Acad. Sci.* **114**, 1811–1816 (2017).

3. C. T. Scott, A. Bekker, C. T. Reinhard, B. Schnetger, B. Krapež, D. Rumble, T. W. Lyons, Late Archean euxinic conditions before the rise of atmospheric oxygen. *Geology*. **39**, 119–122 (2011).

4. C. T. Reinhard, R. Raiswell, C. Scott, A. D. Anbar, T. W. Lyons, A Late Archean Sulfidic Sea Stimulated by Early Oxidative Weathering of the Continents. *Science*. **326**, 713–716 (2009).

5. E. E. Stüeken, D. C. Catling, R. Buick, Contributions to late Archaean sulphur cycling by life on land. *Nat. Geosci.* **5**, 722–725 (2012).

6. L. R. Kump, M. E. Barley, Increased subaerial volcanism and the rise of atmospheric oxygen 2.5 billion years ago. *Nature*. **448**, 1033–1036 (2007).

7. F. Gaillard, B. Scaillet, N. T. Arndt, Atmospheric oxygenation caused by a change in volcanic degassing pressure. *Nature*. **478**, 229–232 (2011).

8. S. L. Olson, C. M. Ostrander, D. D. Gregory, M. Roy, A. D. Anbar, T. W. Lyons, Volcanically modulated pyrite burial and ocean–atmosphere oxidation. *Earth Planet. Sci. Lett.* **506**, 417–427 (2019).

9. O. J. Rouxel, A. Bekker, K. J. Edwards, Iron Isotope Constraints on the Archean and Paleoproterozoic Ocean Redox State. *Science*. **307**, 1088–1091 (2005).

10. N. Planavsky, O. J. Rouxel, A. Bekker, A. Hofmann, C. T. S. Little, T. W. Lyons, Iron isotope composition of some Archean and Proterozoic iron formations. *Geochim. Cosmochim. Acta*. **80**, 158–169 (2012).

11. A. W. Heard, N. Dauphas, Constraints on the coevolution of oxic and sulfidic ocean iron sinks from Archean–Paleoproterozoic iron isotope records. *Geology* (2020), doi:10.1130/G46951.1.

12. B. L. Beard, C. M. Johnson, L. Cox, H. Sun, K. H. Nealson, C. Aguilar, Iron Isotope Biosignatures. *Science*. **285**, 1889–1892 (1999).

13. C. Archer, D. Vance, Coupled Fe and S isotope evidence for Archean microbial Fe(III) and sulfate reduction. *Geology*. **34**, 153–156 (2006).

14. R. Guilbaud, I. B. Butler, R. M. Ellam, Abiotic Pyrite Formation Produces a Large Fe Isotope Fractionation. *Science*. **332**, 1548–1551 (2011).

15. J. M. Rolison, C. H. Stirling, R. Middag, M. Gault-Ringold, E. George, M. J. A. Rijkenberg, Iron isotope fractionation during pyrite formation in a sulfidic Precambrian ocean analogue. *Earth Planet. Sci. Lett.* **488**, 1–13 (2018).

16. N. Dauphas, S. G. John, O. Rouxel, Iron Isotope Systematics. *Rev. Mineral. Geochem.* **82**, 415–510 (2017).

17. J. Marin-Carbonne, C. Rollion-Bard, A. Bekker, O. Rouxel, A. Agangi, B. Cavalazzi, C. C. Wohlgemuth-Ueberwasser, A. Hofmann, K. D. McKeegan, Coupled Fe and S isotope variations in pyrite nodules from Archean shale. *Earth Planet. Sci. Lett.* **392**, 67–79 (2014).

18. J. Marin-Carbonne, V. Busigny, J. Miot, C. Rollion-Bard, E. Muller, N. Drabon, D. Jacob, S. Pont, M. Robyr, T. R. R. Bontognali, C. François, S. Reynaud, M. V. Zuilen, P. Philippot, In Situ Fe and S isotope analyses in pyrite from the 3.2 Ga Mendon Formation (Barberton Greenstone Belt, South Africa): Evidence for early microbial iron reduction. *Geobiology*. **n/a** (2020), doi:10.1111/gbi.12385.

19. E. D. Young, A. Galy, H. Nagahara, Kinetic and equilibrium mass-dependent isotope fractionation laws in nature and their geochemical and cosmochemical significance. *Geochim. Cosmochim. Acta*. **66**, 1095–1104 (2002).

20. N. Dauphas, E. A. Schauble, Mass Fractionation Laws, Mass-Independent Effects, and Isotopic Anomalies. *Annu. Rev. Earth Planet. Sci.* **44**, 709–783 (2016).

21. A. J. McCoy-West, J. G. Fitton, M.-L. Pons, E. C. Inglis, H. M. Williams, The Fe and Zn isotope composition of deep mantle source regions: Insights from Baffin Island picrites. *Geochim. Cosmochim. Acta*. **238**, 542–562 (2018).

22. N. X. Nie, N. Dauphas, R. C. Greenwood, Iron and oxygen isotope fractionation during iron UV photo-oxidation: Implications for early Earth and Mars. *Earth Planet. Sci. Lett.* **458**, 179–191 (2017).

23. N. Dauphas, D. L. Cook, A. Sacarabany, C. Fröhlich, A. M. Davis, M. Wadhwa, A. Pourmand, T. Rauscher, R. Gallino, Iron 60 Evidence for Early Injection and Efficient Mixing of Stellar Debris in the Protosolar Nebula. *Astrophys. J.* **686**, 560–569 (2008).

24. Materials and methods are available as supplementary materials on Science Online.

25. H. Tsikos, A. Matthews, Y. Erel, J. M. Moore, Iron isotopes constrain biogeochemical redox cycling of iron and manganese in a Palaeoproterozoic stratified basin. *Earth Planet. Sci. Lett.* **298**, 125–134 (2010).

26. O. J. Rouxel, A. Bekker, K. J. Edwards, Response to Comment on “Iron Isotope Constraints on the Archean and Paleoproterozoic Ocean Redox State.” *Science*. **311**, 177–177 (2006).

27. A. Bekker, J. F. Slack, N. Planavsky, B. Krapež, A. Hofmann, K. O. Konhauser, O. J. Rouxel, Iron Formation: The Sedimentary Product of a Complex Interplay among Mantle, Tectonic, Oceanic, and Biospheric Processes. *Econ. Geol.* **105**, 467–508 (2010).

28. P. R. Craddock, N. Dauphas, Iron and carbon isotope evidence for microbial iron respiration throughout the Archean. *Earth Planet. Sci. Lett.* **303**, 121–132 (2011).

29. A. Heimann, C. M. Johnson, B. L. Beard, J. W. Valley, E. E. Roden, M. J. Spicuzza, N. J. Beukes, Fe, C, and O isotope compositions of banded iron formation carbonates demonstrate a major role for dissimilatory iron reduction in ~2.5 Ga marine environments. *Earth Planet. Sci. Lett.* **294**, 8–18 (2010).

30. Crosby Heidi A., Roden Eric E., Johnson Clark M., Beard Brian L., The mechanisms of iron isotope fractionation produced during dissimilatory Fe(III) reduction by Shewanella putrefaciens and Geobacter sulfurreducens. *Geobiology*. **5**, 169–189 (2007).

31. J. W. Jamieson, B. A. Wing, J. Farquhar, M. D. Hannington, Neoarchaean seawater sulphate concentrations from sulphur isotopes in massive sulphide ore. *Nat. Geosci.* **6**, 61–64 (2013).

32. S. A. Crowe, G. Paris, S. Katsev, C. Jones, S.-T. Kim, A. L. Zerkle, S. Nomosatryo, D. A. Fowle, J. F. Adkins, A. L. Sessions, J. Farquhar, D. E. Canfield, Sulfate was a trace constituent of Archean seawater. *Science*. **346**, 735–739 (2014).

33. M. C. Koehler, R. Buick, M. A. Kipp, E. E. Stüeken, J. Zaloumis, Transient surface ocean oxygenation recorded in the ~2.66-Ga Jeerinah Formation, Australia. *Proc. Natl. Acad. Sci.*, 201720820 (2018).

34. A. D. Anbar, Y. Duan, T. W. Lyons, G. L. Arnold, B. Kendall, R. A. Creaser, A. J. Kaufman, G. W. Gordon, C. Scott, J. Garvin, R. Buick, A Whiff of Oxygen Before the Great Oxidation Event? *Science*. **317**, 1903–1906 (2007).

35. D. Rickard, G. W. Luther, Chemistry of Iron Sulfides. *Chem. Rev.* **107**, 514–562 (2007).

36. D. Rickard, A. Griffith, A. Oldroyd, I. B. Butler, E. Lopez-Capel, D. A. C. Manning, D. C. Apperley, The composition of nanoparticulate mackinawite, tetragonal iron(II) monosulfide. *Chem. Geol.* **235**, 286–298 (2006).

37. N. Dauphas, A. Pourmand, F.-Z. Teng, Routine isotopic analysis of iron by HR-MC-ICPMS: How precise and how accurate? *Chem. Geol.* **267**, 175–184 (2009).

38. H. Tang, N. Dauphas, Abundance, distribution, and origin of 60Fe in the solar protoplanetary disk. *Earth Planet. Sci. Lett.* **359–360**, 248–263 (2012).

39. H. Tang, N. Dauphas, P. R. Craddock, HIGH PRECISION IRON ISOTOPIC ANALYZES OF METEORITES AND TERRESTRIAL ROCKS: 60Fe DISTRIBUTION AND MASS FRACTIONATION LAWS. *LPS XXXX*. **40**, 1903 (2009).

40. P. R. Craddock, N. Dauphas, Iron Isotopic Compositions of Geological Reference Materials and Chondrites. *Geostand. Geoanalytical Res.* **35**, 101–123 (2011).

41. B. L. Beard, C. M. Johnson, K. L. V. Damm, R. L. Poulson, Iron isotope constraints on Fe cycling and mass balance in oxygenated Earth oceans. *Geology*. **31**, 629–632 (2003).

42. A. E. Isley, Hydrothermal Plumes and the Delivery of Iron to Banded Iron Formation. *J. Geol.* **103**, 169–185 (1995).

43. L. R. Kump, W. E. Seyfried, Hydrothermal Fe fluxes during the Precambrian: Effect of low oceanic sulfate concentrations and low hydrostatic pressure on the composition of black smokers. *Earth Planet. Sci. Lett.* **235**, 654–662 (2005).

44. S. Moorbath, R. K. O'nions, R. J. Pankhurst, Early Archaean Age for the Isua Iron Formation, West Greenland. *Nature*. **245**, 138 (1973).

45. F. Thibon, J. Blichert-Toft, H. Tsikos, J. Foden, E. Albalat, F. Albarede, Dynamics of oceanic iron prior to the Great Oxygenation Event. *Earth Planet. Sci. Lett.* **506**, 360–370 (2019).

46. N. Dauphas, M. van Zuilen, M. Wadhwa, A. M. Davis, B. Marty, P. E. Janney, Clues from Fe Isotope Variations on the Origin of Early Archean BIFs from Greenland. *Science*. **306**, 2077–2080 (2004).

47. A. Angert, S. Rachmilevitch, E. Barkan, B. Luz, Effects of photorespiration, the cytochrome pathway, and the alternative pathway on the triple isotopic composition of atmospheric O2. *Glob. Biogeochem. Cycles*. **17**, 1030 (2003).

48. X. Cao, Y. Liu, Equilibrium mass-dependent fractionation relationships for triple oxygen isotopes. *Geochim. Cosmochim. Acta*. **75**, 7435–7445 (2011).

49. E. D. Young, L. Y. Yeung, I. E. Kohl, On the Δ17O budget of atmospheric O2. *Geochim. Cosmochim. Acta*. **135**, 102–125 (2014).

50. N. E. Levin, T. D. Raub, N. Dauphas, J. M. Eiler, Triple oxygen isotope variations in sedimentary rocks. *Geochim. Cosmochim. Acta*. **139**, 173–189 (2014).

51. A. M. Davis, F. M. Richter, R. A. Mendybaev, P. E. Janney, M. Wadhwa, K. D. McKeegan, Isotopic mass fractionation laws for magnesium and their effects on 26Al–26Mg systematics in solar system materials. *Geochim. Cosmochim. Acta*. **158**, 245–261 (2015).

52. J. Farquhar, D. T. Johnston, B. A. Wing, K. S. Habicht, D. E. Canfield, S. Airieau, M. H. Thiemens, Multiple sulphur isotopic interpretations of biosynthetic pathways: implications for biological signatures in the sulphur isotope record. *Geobiology*. **1**, 27–36 (2003).

53. S. Ono, B. Wing, D. Johnston, J. Farquhar, D. Rumble, Mass-dependent fractionation of quadruple stable sulfur isotope system as a new tracer of sulfur biogeochemical cycles. *Geochim. Cosmochim. Acta*. **70**, 2238–2252 (2006).

54. D. T. Johnston, J. Farquhar, K. S. Habicht, D. E. Canfield, Sulphur isotopes and the search for life: strategies for identifying sulphur metabolisms in the rock record and beyond. *Geobiology*. **6**, 425–435 (2008).

55. J. Zhang, S. Huang, A. M. Davis, N. Dauphas, A. Hashimoto, S. B. Jacobsen, Calcium and titanium isotopic fractionations during evaporation. *Geochim. Cosmochim. Acta*. **140**, 365–380 (2014).

56. A. Kappler, C. Pasquero, K. O. Konhauser, D. K. Newman, Deposition of banded iron formations by anoxygenic phototrophic Fe(II)-oxidizing bacteria. *Geology*. **33**, 865–868 (2005).

57. K. O. Konhauser, N. J. Planavsky, D. S. Hardisty, L. J. Robbins, T. J. Warchola, R. Haugaard, S. V. Lalonde, C. A. Partin, P. B. H. Oonk, H. Tsikos, T. W. Lyons, A. Bekker, C. M. Johnson, Iron formations: A global record of Neoarchaean to Palaeoproterozoic environmental history. *Earth-Sci. Rev.* **172**, 140–177 (2017).

58. J. Farquhar, H. Bao, M. Thiemens, Atmospheric Influence of Earth's Earliest Sulfur Cycle. *Science*. **289**, 756–758 (2000).

Acknowledgments: Discussions with Stephanie Olson and Jake Waldbauer were appreciated. Nigel Brauser and Anne Davis are thanked for comments on the clarity of the manuscript. This work was funded by NASA grants 80NSSC17K0744 to ND and AWH (Habitable Worlds), 359NNX17AE86G to ND (LARS), and NNX17AE87G to ND (Emerging Worlds). Participation by AB was supported by NSERC Discovery and Acceleration grants.

List of Supplementary Materials:

Materials and Methods
Supplementary Text
Figs. S1 to S7
Tables S1 to S4

Figures

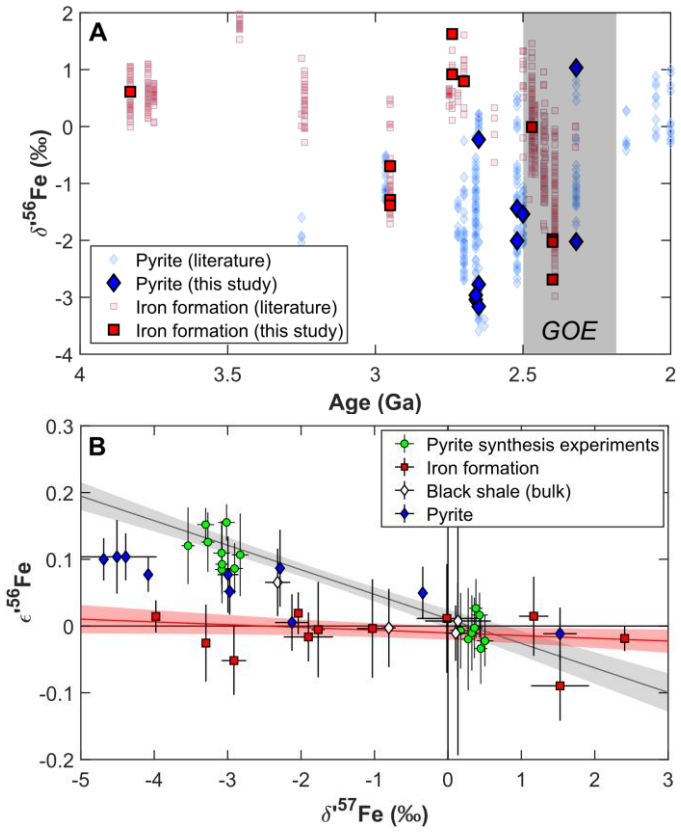

Fig. 1.

Iron isotope systematics of pre-GOE sediments and pyrites, and pyrites produced in laboratory experiments. A) $\delta'^{56}Fe$ values of IFs and pyrites analyzed in this study, plotted against their ages on the horizontal axis, relative to published IF and pyrite data. B) Triple-Fe-isotope systematics for IFs, pyrites, and black shales in $\epsilon'^{56}Fe$ *vs.* $\delta'^{57}Fe$ space. Error bars and envelopes are 95% confidence intervals. The slopes of endmember MFLs associated with iron-redox processes, and KIEs during pyritization, are constrained through analysis of isotopically light Mn-rich IFs and laboratory pyrite precipitation via the H_2S pathway (*14*, *24*, *35*), respectively. The slope of the IF MFL agrees with the theoretical equilibrium law (defined by the horizontal axis at $\epsilon'^{56}Fe = 0$), implying control by Fe^{2+}-Fe^{3+} equilibrium (*20*, *22*). Pyrite synthesis defines a kinetic MFL for pyrite precipitation. Pre-GOE pyrites fall in an intermediate space between redox equilibrium and kinetic endmembers.

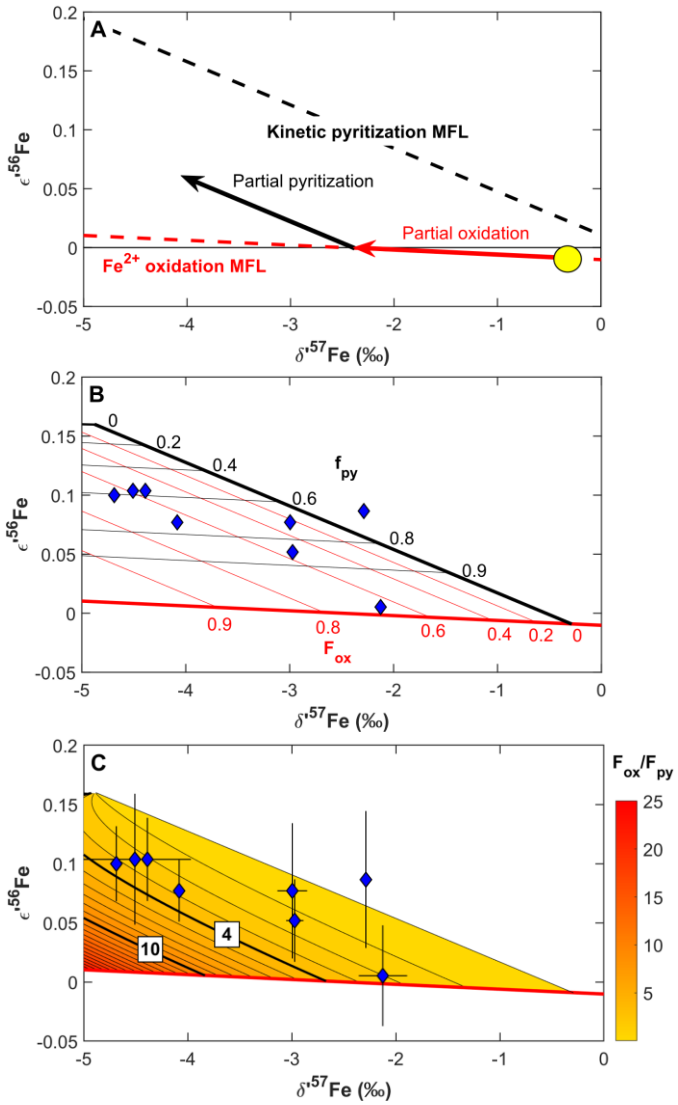

Fig. 2.

Interpreting triple-Fe-isotopic signatures of isotopically light pyrites. A) Schematic of two-step process involved in pyrite formation. Iron with starting compositions resembling hydrothermal fluids (gold circle) is oxidized, driving residual Fe^{2+} to light compositions along the Fe^{2+} oxidation MFL. Partial pyrite precipitation from this Fe^{2+} subsequently causes fractionations along the kinetic pyrite formation MFL. The approach is detailed in Figure S4 and equations in (*24*). B) Pyrite data and contours for F_{ox} and f_{py} in triple Fe isotope space. F_{py}, the fraction of total upwelled Fe deposited in pyrite, is calculated as $F_{py} = f_{py} \times (1 - F_{ox})$. C) Pyrite data and contours of F_{ox}/F_{py} (relative size of oxic and pyrite sedimentary Fe sinks). Bold contours at 4 and 10 indicate thresholds for net O_2 source vs. sink behavior for volcanic H_2S/SO_2 inputs ratios of 1 (*7*) and 0 (*8*), respectively.

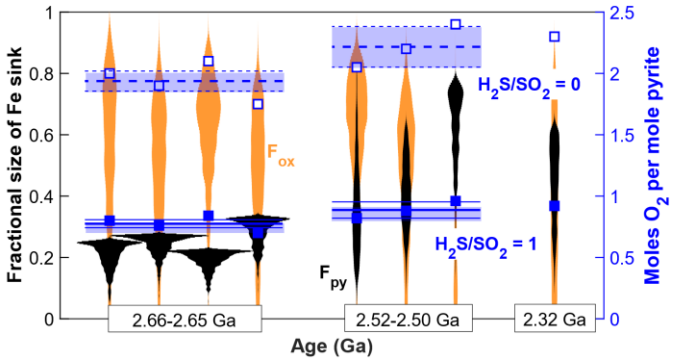

Fig. 3

D) F_{ox} and F_{py}, and molar O_2 yield estimates, from Monte Carlo error propagation. Violin plots for F_{ox} and F_{py} probability densities for results determined from propagation of errors on the $\epsilon'^{56}Fe$ and $\delta'^{57}Fe$ values for each measured pyrite and the errors on the slopes of the MFLs (*24*). Blue filled (open) squares: Estimated molar O_2 yields per mole of pyrite buried for individual samples for H_2S/SO_2 input ratios of 1 (0). Blue (dashed) lines and shaded areas: mean molar O_2 yield for H_2S/SO_2 input ratios of 1 (0) and 95 % confidence interval for pyrites grouped by age interval.

Science
AAAS

Supplementary Materials for

Resolving the Role of Ocean Iron Sinks in Early Atmospheric Oxygenation

Andy W. Heard, Nicolas Dauphas, Romain Guilbaud, Olivier J. Rouxel, Ian B. Butler, Nicole X. Nie, Andrey Bekker

Correspondence to: andyheard@uchicago.edu

This PDF file includes:

Materials and Methods
Supplementary Text
Figs. S1 to S7
Tables S1 to S4

Materials and Methods

Methods

Pyrite synthesis experiments

To constrain the triple Fe isotopic expression of pyrite precipitation, pyrite was synthesized at the University of Edinburgh, via the FeS-H_2S pathway following the methodology of Guilbaud et al. (2011) (*14*) and references therein, which have consistently been demonstrated to produce pyrite precipitates from an FeS_m (mackinawite) reactant. All reagents were of analytical grade, and solutions were prepared using 18 MΩcm deionized water and sparged for 30 min with O_2-free grade N_2 before use. Solutions were prepared and solid FeS_m was synthesized in N_2-filled recirculating Saffron alpha anoxic chamber under O_2-free conditions. FeS_m was precipitated by mixing 100 mL of 0.6 M iron (Fe^{2+}) solution prepared with Mohr's salt ($(NH_4)_2Fe(SO_4)_2 \cdot 6H_2O$; Sigma Aldrich) with 100 mL of 0.6 M sulfide solution made with $Na_2S \cdot 9H_2O$ (Sigma Aldrich). This reaction produced a black precipitate. The precipitate was filtered using a Buchner filter with Whatman™ No. 1 filter paper, resuspended in sparged water and the filtration was repeated three times. The freshly precipitated FeS_m was freeze-dried overnight on a Mini-Lyotrap (LTE) freeze-dryer then transferred back to the anoxic chamber and stored under O_2-free conditions until use. The low-metal complexing MOPS (3-(N-morpholino)propanesulfonic acid) buffer (3-N-morpholinopropanesulfonic acid, pKa = 7.31, Fisher) was made by dissolution of its sodium salt and in sparged water, buffered to pH 6 by NaOH titration. Ti^{3+} citrate was prepared by adding 5 mL 15% $TiCl_3$ to 50 mL 0.2 M Na citrate and buffered to pH 7 with Na_2CO_3. The solutions were stored in the glove box under O_2-free conditions until use.

The pyrite precipitation experiments were prepared in the glove box. Approximately 300 mg of the freeze-dried FeS_m was weighed into serum bottles, 10 mL of 0.05 M MOPS buffer solution was added, and the bottles were sealed with rubber stoppers and aluminum crimper seals. The sealed bottles were attached to a gas transfer manifold via a hypodermic needle inserted through the rubber stopper, and the manifold and reaction bottle were flushed with O_2-free grade N_2 and pumped down to -14 PSI (-97 kPa, at full vacuum) three times. A sealed serum bottle containing 800 mg solid $Na_2S \cdot 9H_2O$ was attached to the manifold via a hypodermic needle and flushed and pumped three times. A syringe was used to inject 2 mL of sparged, 50 vol% H_2SO_4 into the $Na_2S \cdot 9H_2O$-containing bottle to generate H_2S. After H_2S transfer into the FeS_m-containing serum bottle, the pressure was adjusted to slight under-pressure (~ -2.5 PSI or ~ -17 kPa) by N_2 addition. The needle holes in the serum bottle septa were covered with silicone sealant and transferred to a 40°C oven to allow the pyrite precipitation reaction to take place. After different, pre-determined reaction durations, the serum bottle reaction vessels were removed from the oven and frozen to stop the reaction.

Once frozen, the serum bottles were unsealed under flushing N_2 and excess H_2S in the headspace was removed. The bottles were then re-stoppered, the stoppers pierced with a hypodermic needle under flushing N_2, and the bottles left in the freeze-dryer for a day. The freeze-dried serum bottles were transferred to the anoxic chamber, and 2 mL sparged water and a few drops of the Ti^{3+} citrate were added to poise the Eh at low negative values to prevent FeS_m oxidation and ensure full dissolution of FeS_m in a preferential dissolution protocol developed by Rickard et al. (2006) (*36*) and modified and calibrated by Guilbaud et al. (2011) (*11*). The serum bottles were resealed and placed to a fume hood for preferential dissolution. In the fume hood, 20 mL of sparged 1.2 M HCl was injected into the serum bottle via hypodermic syringe to fully dissolve only FeS_m and MOPS salt. Remaining solids, essentially pyrite, were separated by filtering on a 0.45 µm Millipore filter, and rinsing with sparged water. The FeS_m in HCl solutions

were adjusted to 50 mL by addition of water and a 10 mL (20%) cut was dried down in clean Savillex Teflon beakers for transport and isotopic analysis. Pyrite was dissolved with drops of concentrated HNO_3, solutions were adjusted to 50 mL by addition of water and a 10 mL (20%) cut was dried down in clean Savillex Teflon beakers for transport and isotopic analysis. A 20 mL cut was taken for pyrite samples SB5 Py and SB6 Py, which were produced in short (4.66 hours) duration experiments and for which low pyrite iron yields were anticipated. In the Origins Laboratory at the University of Chicago, samples were dissolved in Aqua Regia with drops of 11 M $HClO_4$ at 140°C, and dried down twice, then treated three times with 2 mL of H_2O_2 to remove organic carbon salts left in the FeS_m solutions by MOPS. The solutions were then re-dissolved in 5 mL 6M HCl ready for iron purification. A small (5 µL) aliquot of each solution was dried down and redissolved in 0.3 M HNO_3 to check the iron concentration of these solutions using MC-ICP-MS and determine the correct amount of volume of each sample solution to be passed through iron purification.

Analytical methods

Analytical procedures for iron purification and isotopic measurements followed standard procedures used at the Origins Laboratory at the University of Chicago (*22*, *37–40*). Samples were prepared from powders of black shale and IF material, and hand-picked pyrite grains. Sample masses ranged from 12-22 mg, 2-6 mg, and 13-84 mg for black shale, IF, and pyrite grains respectively. Samples were digested in clean Savillex Teflon beakers. First, 1 ml 28 M HF + 0.5 ml 15 M HNO_3 + a few drops 11 M $HClO_4$ was added, and closed beakers were heated at 130 ºC. Samples were evaporated to dryness and re-dissolved in Aqua Regia (0.75 ml 11 M HCl + 0.25 ml 15 M HNO_3) and a few drops 11 M $HClO_4$, before heating and evaporation was repeated. The Aqua Regia + $HClO_4$ step was repeated 3 times to release all iron to solution. Samples were evaporated to dryness and 0.5 ml of 6 M HCl or 10 M HCl was added, depending on the purification procedure to be used. Larger volumes of the same acid were used for digestion of pyrite grains, which contained greater masses of Fe. Iron purification made use of both the standard 'short column' procedure, which is now routine in the Origins Laboratory (*37*, *40*), and a 'long column' procedure designed to more effectively eliminate Cu from the matrix (*38*, *39*), which was a concern for sulfide samples.

Short column iron purification: Disposable Bio-Rad Poly-Prep polyethylene columns were filled with 1 ml of AG1-X8 200-400 mesh Cl-form anion exchange resin. The resin was pre-conditioned with 10 ml of MilliQ H_2O, 5 ml of 1 M HNO_3, 10 ml of MilliQ H_2O, 9 ml of 0.4 M HCl, 5 ml of MilliQ H_2O, and 2 ml of 6 N HCl. Samples were loaded onto columns in 0.25 ml of 6 M HCl. Matrix and interfering elements were eliminated by passing 8 ml of 6 M HCl through the column. Iron was eluted with 9 ml of 0.4 M HCl and recovered in clean Teflon beakers. Samples were evaporated to dryness and redissolved in 0.25 ml of 6 M HCl, before repeating the column procedure a second time with new resin. All experimentally synthesized pyrite and FeS_m samples were also purified using this procedure.

Long column iron purification: This alternative iron purification procedure was developed to eliminate Cu as a potentially significant matrix element associated with sulfide phases. Reusable 30 ml Savillex Teflon columns with a 0.64 cm ID capillary cut to 10.5 cm length were loaded with 3 ml of AG1-X8 anion exchange resin. The resin was preconditioned with 10 ml MilliQ H_2O, 10 ml 0.4 M HCl, 5 ml MilliQ H_2O, 10 ml 0.4 M HCl, and 4 ml of 4 ml of 10 M HCl. Samples were loaded onto columns in 0.25 ml of 10 M HCl. Matrix and interfering elements were eliminated by passing 4.5 ml of 10 M HCl, and 30 ml of 4 M HCl, the latter to eliminate Cu in particular. Iron

was eluted with 9 ml of 0.4 M HCl and recovered in clean Teflon beakers. Samples were evaporated to dryness and redissolved in 0.25 ml of 10 M HCl, before repeating the column procedure with new resin.

Iron isotopic compositions were measured on a Neptune MC-ICP-MS at the University of Chicago. Analyses were made of the extent of isotopic fractionation (δ values), and the departure from a reference mass-dependent fractionation law (ϵ). The Fe isotopes at masses 54, 56, 57, and 58 were measured simultaneously along with ^{53}Cr and ^{60}Ni for correction of ^{54}Cr and ^{58}Ni interferences on ^{54}Fe and ^{58}Fe respectively. The ^{53}Cr and ^{60}Ni interferences were corrected for using the exponential law. All of the Fe isotopes have molecular interferences with argide ions ($^{40}Ar^{14}N^+$, $^{40}Ar^{16}O^+$, $^{40}Ar^{16}O^1H^+$, and $^{40}Ar^{18}O^+$), which present a significant hindrance to obtaining the requisite precision to resolve mass-dependent fractionation laws. Therefore, measurements were made on the flat-topped peak shoulder in high-resolution mode using a standard Neptune entrance slit. A few sample analyses made use of 'ultra-high-resolution mode' utilizing the high-resolution mode of a Thermo Element 2 entrance slit. Results were consistent with those obtained using the standard HR method, but offered no improvement in precision whilst requiring higher iron concentrations to obtain the same signal. Nickel or aluminum sampler and H skimmer cones were used. Standard-sample bracketing was used to correct isotopic ratio measurements for instrumental mass fractionation, and Fe isotopic ratios of samples are reported relative to the average isotopic ratios of the bracketing standard solutions of IRMM-524, which has an identical isotopic composition to IRMM-014. The exponential law was initially used to calculate ϵ values by fixing $^{57}Fe/^{54}Fe$ to 0.362549, the value of IRMM-014. The δ and ϵ values of samples are given by

$$\delta = \left[\left({}^{i}Fe/{}^{54}Fe\right)_{sample}/\left({}^{i}Fe/{}^{54}Fe\right)_{std} - 1\right] \times 10^3,$$

$$\epsilon = \left[\left({}^{i}Fe/{}^{54}Fe\right)^{*}_{sample}/\left({}^{i}Fe/{}^{54}Fe\right)^{*}_{std} - 1\right] \times 10^4,$$

where i = 56, 57, or 58 and the * indicates ratios corrected for mass fractionation by internal normalization to a fixed reference $^{57}Fe/^{54}Fe$ ratio using the exponential law(*17*, *20*),

$$\ln\left({}^{i}Fe/{}^{54}Fe\right)^{*}_{sample,\ corrected} = \ln\left({}^{i}Fe/{}^{54}Fe\right)_{sample,\ measured} - \ln\frac{\left({}^{57}Fe/{}^{54}Fe\right)_{sample,\ measured}}{\left({}^{57}Fe/{}^{54}Fe\right)_{fixed\ reference}}\frac{\ln\left(m_{i_{Fe}}/m_{54_{Fe}}\right)}{\ln\left(m_{57_{Fe}}/m_{54_{Fe}}\right)}$$

Bracketing standards are also internally normalized using the same exponential law. Subsequent to measurements, data were renormalized to the high-temperature equilibrium limit law for display, to fit the common convention used with other isotope systems. Data normalized to the exponential law are also presented in Tables S1 and S2, and a version of Figure 1B using this normalization is also presented in Figure S1.

Samples and standards were measured in 0.3 M HNO_3 and introduced into the plasma torch using a Cetac Aridus II or ESI Apex Omega desolvating nebulizer system with no auxiliary N_2 flow. On-peak zero was determined at the start of each measurement sequence by analyzing a clean aliquot of the same HNO_3 in which samples were measured. Sample and standard concentrations between 5 ppm and 30 ppm were used in different measurement sessions depending on sensitivity and the entrance slit being used, but most analyses making use of 10-12 ppm iron sample and standard solutions. Measurements were made with the use of bracketing standards matched to sample concentrations within ± 5 %. Measurements of ^{56}Fe were made on a 10^{10} Ω amplifier resistor because signal intensities were generally higher than 50 V, and 10^{11} Ω amplifier resistors were used for measurement of ^{54}Cr, ^{54}Fe, ^{57}Fe, ^{58}Fe, and ^{60}Ni.

For experimentally synthesized samples, the mass-dependent Fe isotopic fractionation ($\delta^{56}Fe$) was also determined by standard Fe isotopic analytical methods. A quartz cyclonic spray chamber was used to introduce 1 ppm solutions into the Neptune operating in medium resolution mode, resulting in a signal of ~7 V. Isotopic compositions were determined by standard-sample bracketing. All Fe isotopic analyses of experimentally synthesized samples (both triple isotopic and conventional) were normalized to IRMM-524 during analyses, but subsequently renormalized to the measured isotopic compositions of the starting batches of FeS_m material used in respective experiments. All errors were combined in quadrature as appropriate. The average fractionation factor we determined for the pyrite precipitation reaction was $\alpha_{FeS\text{-}pyrite} = 1.0023 \pm 0.0003$ (95% C.I.), consistent with the results of Guilbaud et al. (2011) (*14*). This fractionation factor was determined by calculating the average difference between the FeS_m and pyrite splits from each serum bottle experiment. The degree of pyritization (DOP – the fraction of the total Fe in the pyrite pool) was calculated from the total iron masses in each split indicated by concentration measurements and known dilution factors. The low DOP values (max ~14 %) obtained in our experiments were not conducive to fitting the data to a Rayleigh distillation trend, however the distance between linear trends plotted through $\delta^{56}Fe$ *vs.* degree of pyritization for the FeS_m and pyrite data also gave an average fractionation factor of $\alpha_{FeS\text{-}pyrite} = 1.0023$ (Fig. S2).

We saw no systematic difference between short and long column purification techniques in triple Fe isotopic data for IF sample JD-C165A, and pyrite sample SF-1 599.8 Py, which were each processed multiple times using either column procedure to check the reproducibility of our measurements in the absence of geostandard materials, which have been analyzed to this level of precision (Fig. S2). In all cases, the individual pyrite analyses for this repeat sample have $\epsilon^{56}Fe$ values that significantly more positive than the value of the anticipated for IF with the same $\delta^{57}Fe$ value (Fig. S2). In addition, as a check for possible matrix effects in the preparation of IF and pyrite samples, we performed a matrix test with IRMM-524 standard iron solution. Briefly, aliquots of an IF sample (REX 187.5) and a pyrite sample (SF-1 623.6 Py) were passed through the short column purification procedure and the eluted matrix from each was collected. These matrix cuts were further purified by being passed through this column chemistry procedure again. These matrix cuts were mixed with a solution of IRMM-524 back to the original iron concentration, and the iron was purified with two passes on short columns in the same manner as other samples. The $\epsilon^{56}Fe$ values of both matrix-adjusted solutions and a pure solution of IRMM-524 were within error of zero and all identical within error (Fig. S2), suggesting that sample matrices did not systematically affect our $\epsilon^{56}Fe$ analyses.

Modeling methods - Calculation of oxic and sulfidic sink sizes

Triple Fe isotopic systematics allow the isotopic composition of any given isotopically depleted pyrite to be deconvolved into contributions from KIE during pyrite precipitation, and isotopic depletion in dissolved Fe^{2+} resulting from the removal of isotopically heavy Fe^{3+} (oxyhydr)oxides. Rough estimates for those contributions can be solved graphically (Fig. 2A), however the uncertainty on those estimates requires propagation of all uncertainties on both the KIE and oxidation MFLs, in addition to uncertainty of individual pyrite measurements. This error propagation was performed using a Monte Carlo method in a MATLAB script.

For each pyrite and IF datapoint, an array of simulated datapoints was generated by randomly sampling 1000 times from a normal distribution defined by the 95 % C.I. of the measured $\epsilon'^{56}Fe$ and $\delta'^{57}Fe$ values and standard deviations. From the 1000 sets of randomly generated IF datapoints, 1000 MFLs were generated by linear regression to encompass the anticipated range of seawater

Fe^{2+} evolutions in $\epsilon'^{56}Fe$ *vs.* $\delta'^{57}Fe$ space that could be driven by Fe^{3+} (oxyhydr)oxide removal. An array of 1000 values for the kinetic slope was generated by randomly sampling 1000 times from a normal distribution defined by the 95 % C.I. of the experimentally determined slope. The intercept of a line with the kinetic slope passing through the pyrite $\epsilon'^{56}Fe$ *vs.* $\delta'^{57}Fe$, with the MFL fitted to the IF data, was found by solution of simultaneous equations (Fig. S4). The IF line, and the line defining the KIE trajectory which connects pyrite datapoints to the IF line, are given respectively by the equations:

$$\epsilon'^{56}Fe = a_{ox}\delta'^{57}Fe + b_{ox}$$

$$\epsilon'^{56}Fe = a_{KIE}\delta'^{57}Fe + b_{KIE}$$

where a is the empirically determined slope of the MFL, and b is the intercept with the vertical axis. For known $\epsilon'^{56}Fe$ and $\delta'^{57}Fe$ values of a given pyrite, the second equation can be rearranged as:

$$b_{KIE} = \epsilon'^{56}Fe_{\ py} - a_{KIE}\delta'^{57}Fe_{py}$$

The intercept with the IF MFL is then found by equating the line equations, giving (after substitution):

$$\delta'^{57}Fe_{int} = \frac{\left(\epsilon'^{56}Fe_{\ py} - a_{KIE}\delta'^{57}Fe_{py} - b_{ox}\right)}{\left(a_{ox} - a_{KIE}\right)}$$

where the subscript $_{int}$ refers to the value at the intercept (note in the main text this is denoted with the subscript $_{wo}$) (Fig. S4). The $\delta'^{57}Fe$ value at the intercept with the IF MFL ($\delta'^{57}Fe_{int}$) was taken as the isotopic composition of the pyrite-forming water mass that had already undergone iron oxidation, and the magnitude of the KIE during pyritization was calculated as the difference between the intercept value and the $\delta'^{57}Fe$ of pyrite. This exercise was repeated 1000 times for each depleted pyrite sample using the randomly generated values of all parameters described. We note that in the Main Text, the discussion focusses on $\delta'^{56}Fe$ values as these are more commonly reported in the literature, but here the exact procedure is detailed as performed, and conversion between $\delta'^{57}Fe$ and $\delta'^{56}Fe$ values is done by dividing by the values of $\theta^{56/57}$ presented in this study.

The extent of Fe^{2+} oxidation (F_{ox}) to give a certain $\delta'^{57}Fe_{int}$ was calculated using a Rayleigh distillation model:

$$\delta'^{57}Fe_{int} = \delta'^{57}Fe_{i} + 1000(\alpha - 1)\ln(1 - F_{ox})$$

where α is the fractionation factor during in Fe^{2+} oxidation and precipitation that gives fractionation $1000\times(\alpha\text{-}1) = 0.5$ ‰/amu during Fe^{3+} (oxyhydr)oxide removal (*16*), the subscript $_i$ denotes the starting $\delta'^{57}Fe$ for a hydrothermal Fe^{2+} source of ~-0.3 ‰ (*9*, *41*). Iterations where the inferred $\delta'^{57}Fe$ of seawater was more positive than this value were rejected as they would imply a negative degree of Fe^{2+} oxidation.

The fraction of pyrite precipitation (F_{py} in Main Text) was also determined in a Rayleigh distillation model. We calculate f_{py} by assuming that bulk pyrite nodules represent the cumulative product of pyrite precipitated from the initial Fe^{2+} pool. This contrasts with in situ measurement of individual nodule layers that better approximate instantaneous precipitate compositions during the growth of pyrite grains (*17*, *18*). The magnitude of the KIE that was expressed in the product was calculated as the difference between the product and initial reactant:

$$\delta'^{57}Fe_{py} - \delta'^{57}Fe_{int} = \frac{\left(F_{py} - 1\right) \times 1000(\alpha - 1)\ln\left(1 - F_{py}\right)}{F_{py}}$$

where we assumed the maximum fractionation during pyrite precipitation (via FeS_m) from Fe^{2+} of $1000\times(\alpha\text{-}1) = -1.55$ ‰/amu. Iterations requiring a larger instantaneous fractionation were rejected. The value of F_{py} was determined by solving this equation numerically. The cumulative product composition cannot evolve past the initial composition of the reactant reservoir, when the reactant reservoir has been completely consumed. Therefore, iterations requiring a positive offset of the pyrite datapoint from δ'^{57}Fe of seawater were rejected. Once the 1000 iterations for calculation of F_{ox}, and F_{py}, had been completed, the fractional size of the sulfidic sink (F_{ss} in Main Text) was calculated as $F_{py} \times (1 - F_{ox})$ for each pyrite with a confidence interval dictated by the range of values generated in the 1000 iterations. Monte Carlo simulation estimates of F_{py} and F_{ox} for each pyrite sample spanned a large range, but these variations were strongly correlated (Fig. S5). This is because a more negative estimate for the isotopic composition of seawater (which implies a larger F_{ox}), gives a smaller estimate for the fractionation during the precipitation of pyrite from the oceanic iron pool (which implies a larger F_{py}). These two effects have an opposite impact on the estimate of F_{ss}, therefore, F_{ss} estimates vary less than F_{ox} or F_{py}.

Triple-Fe-isotope-derived F_{ox} and F_{py} from pyrites can also be used to estimate the relative fluxes of Fe^{2+} and S (as SO_4^{2-}, H_2S, and S_8) to shelf environments in the Neoarchean and pre-GOE Paleoproterozoic. Assuming an FeS_2 stoichiometry for sedimentary sulfide, the Fe/S ratio in the shelf sediments is given by $(Fe/S)_{sed} = [F_{py} + F_{ox}]/[2 \times F_{py}]$, where F_{py} and F_{ox} are calculated based on the triple-Fe-isotopic measurements presented above. We only consider the relative magnitude of oxide and sulfide iron sinks (e.g., iron silicates or carbonates are not considered) because they are the only ones that have large known isotopic effects, and that can influence redox balance in the Archean. Central estimates of $(Fe/S)_{sed}$ have a range of 0.7 to 2.0 across all samples (Table S4). The Jeerinah and Lokammona formation pyrites have $(Fe/S)_{sed} \geq 1.3$, while younger pyrites deposited shortly before the GOE have lower ratios. For comparison, the ratio of modern Fe input from continental weathering (0.4 Tmol/yr) and hydrothermal venting at mid-ocean ridges (0.18 Tmol/yr) (*42*), to subaerial volcanic SO_2 emissions (0.4-1.4 Tmol/yr) (*3*), continental weathering supply of SO_4^{2-} (11 Tmol/yr) (*42*), and hydrothermal H_2S supply (0.17 Tmol/yr) (*42*), is approximately 0.05. The Neoarchean-Paleoproterozoic pyrite record thus suggests a ratio of Fe to S supply to the oceans 14-40 times greater than modern. Archean hydrothermal and continental Fe^{2+} fluxes exceeded modern levels, due to higher mantle heat flow (*42*), low sulfate content in the ocean (*43*), and continental weathering in contact with anoxic atmosphere. On another hand, the weathered SO_4^{2-} flux and hydrothermal H_2S flux (*43*) were lower throughout the Archean. Our calculated $(Fe/S)_{sed}$ values do not necessarily require weaker Archean volcanic SO_2 fluxes than now, but they indicate that locally developed euxinic conditions (*3*, *4*, *8*) are not representative of the global ocean iron cycle where the burial of Fe^{3+}-(oxyhydr)oxides was the dominant iron sink. For ca. 2.5 Ga pyrites, an additional source of sulfate from oxidative weathering of continental sulfides (*4*) might explain why $(Fe/S)_{sed}$ values are lower relative to those in the older Jeerinah and Lokammona formations (Table S4).

Sample Materials

Geological setting and age constraints for shale-hosted pyrite samples are given by Rouxel et al. (2005) (*6*). Ages and geological units for all samples in this study are provided in Table S3. References for age constraints for pyrite and shale samples, and most IF samples, are provided in Rouxel et al. (2005; 2006) (*6*, *23*), and Planavsky et al. (2012) (*7*), respectively. Age data for samples from the Hotazel Formation and Isua Supracrustal Belt IFs are provided by Gumsley et

al. (2017) (*2*), and Moorbath et al. (1973) (*44*), and the geologic setting and Fe isotopic systematics of these IF have been discussed in the literature elsewhere (*25*, *45*, *46*).

Pyrite grains from organic rich shales, a few bulk organic rich shales, and bulk IF samples were selected for this study. Pyrite grains and bulk shales were sampled from a subset of drill core samples previously studied for Fe isotopic variations by Rouxel et al. (2005; 2006) (*9*, *26*), New pyrite grains were picked at the University of Hawaii. The nature of these grains was described in detail by Rouxel et al. (2005) (*6*). Pyrite grains in organic-rich shales that were subsampled in our study occurred as nodules ~ 1 mm to 1 cm in diameter, with C-rich inclusions in variable amounts. The nodular pyrite either had no internal structure, or was composed of concentrically laminated, fine-grained pyrite or bladed pyrite crystals. Euhedral pyrite crystals commonly overgrew the outer part of the nodules. Shale lamina typically bends around pyrite nodules, which supports interpretations of their origins as being formed early on during diagenesis. Pyrite nodules often display complex features such as multiple-growth bands or composite nodules formed by coalescence of several nodules. Dissolution and reprecipitation of primary sulfide nodules could have happened in some samples and likely resulted in formation of massive pyrite, often characterized by euhedral grains free of C-rich inclusions.

Localized dissolution-reprecipitation is unlikely to have affected Fe-isotopic compositions of pyrites. In the large numbers of samples analyzed per formation by Rouxel et al. (2006) (*9*) strongly negative δ^{56}Fe values were a consistent feature and no link between Fe isotopic composition and the nature of individual pyrite grains was reported, which supports the notion that these are primary sedimentary signatures and not the results of later alteration of the host rocks. Heard and Dauphas (2020) (*11*) recently discussed the fidelity of the pyrite Fe isotope record as an archive of primary sedimentary signatures. In brief, the resistance of this system to metamorphic overprinting due: to the high abundance of Fe, low solubility of pyrite and small size of Fe isotopic fractionations at metamorphic temperatures all make it unlikely that primary sedimentary Fe isotopic signatures have been compromised by secondary processes that may nonetheless have affected the texture of pyrite grains. In practice, Marin-Carbonne et al. (2020) (*18*) recently demonstrated through in situ work that Archean pyrites that experienced late fluid circulation that led to partial recrystallization and alteration of S isotopic systematics, did not modify the Fe isotopic composition, in line with our expectations outlined above.

Supplementary Text

Background on mass fractionation laws for Fe isotopes

Instantaneous fractionations

Numerous reaction pathways have been proposed to create the >4 ‰ δ^{56}Fe range in Archean IFs, shales, and pyrites. The extent of Fe isotopic fractionation is insufficient to discriminate between different scenarios for sedimentary iron cycling in the Archean oceans, because many fractionation processes can generate a large and indistinguishable range in delta values. Considering two isotopic ratios could resolve this ambiguity, because the slope of δ^{56}Fe *vs*. δ^{57}Fe reflects the mass fractionation law (MFL) governing a process, and this law may be distinct for the fractionation processes at the root of various scenarios proposed for the Archean Fe isotopic record. Mass-dependent fractionation is described with a power law

$$^{56}\alpha_{A/B} = {}^{57}\alpha_{A/B}{}^{\theta^{56/57}}$$

where $^{x}\alpha_{A/B}$ are fractionation factors for isotope x between reservoirs A and B, and $^{56/57}\theta$ is the mass dependent exponent or slope in triple Fe isotope space (*20*). Natural processes imparting

different slopes of MFLs in three-isotope diagrams have been identified for O (*47–50*), Mg (*19*, *51*), S (*52–54*), Ca (*55*), Ti (*55*), and Fe (*21*, *22*), but this has yet to be investigated for Fe isotopes in sedimentary rocks with sufficient precision to resolve distinct slopes. The slope $\theta^{56/57}$ for the triple-Fe-isotope diagram is given by

$$\theta^{56/57} = \frac{\delta'^{56}\mathrm{Fe}}{\delta'^{57}\mathrm{Fe}} = \frac{\ln\left(\left(\frac{^{56}\mathrm{Fe}}{^{54}\mathrm{Fe}}\right)\Big/\left(\frac{^{56}\mathrm{Fe}}{^{54}\mathrm{Fe}}\right)_{\mathrm{std}}\right)}{\ln\left(\left(\frac{^{57}\mathrm{Fe}}{^{54}\mathrm{Fe}}\right)\Big/\left(\frac{^{57}\mathrm{Fe}}{^{54}\mathrm{Fe}}\right)_{\mathrm{std}}\right)},$$

where δ’ is related to the standard δ notation by

$$\delta' = 1000\times\ln\left((\delta/1000)+1\right).$$

Slopes vary only subtly between MFLs and therefore it is convenient for the purposes of visualization to express one isotopic ratio in terms of its deviation from an arbitrary reference law in parts per 10,000 by using ϵ’ notation (*20*, *22*) where

$$\epsilon'^{56}\mathrm{Fe} = \left[\delta'^{56}\mathrm{Fe} - 0.672\times\delta'^{57}\mathrm{Fe}\right]\times 10.$$

In ϵ'^{56}Fe *vs.* δ'^{57}Fe diagrams MFLs are straight lines, and when the high-temperature equilibrium limit law with $\theta^{56/57}$ = 0.678 is used as the reference law, ϵ'^{56}Fe values are 0 if fractionation follows the exponential law. Other MFLs have positive (negative) slopes if $\theta^{56/57}$ is larger (smaller) than 0.678.

These laws describe mass-dependent fractionation in a single step process. This approach is an oversimplification in cases where isotopes have been fractionated via several geochemical pathways, via Rayleigh distillation, or where samples reflect mixtures of two (or more) isotopically distinct pools of the element of interest. These concerns are well-documented in the more mature field of triple O and S isotope study (*47–49*, *52–54*), but we show here that these concerns are of diminished importance in application to low-temperature Fe isotope systematics. This is because both Rayleigh distillation and mixing produce curves in ϵ'^{56}Fe *vs.* δ'^{57}Fe space that are practically indistinguishable from instantaneous MFLs over the natural range of Fe isotopic variations.

Rayleigh distillation

In the case of Rayleigh distillation, Ono *et al.* (*53*) have shown that the closed-system evolution of a reactant reservoir (A) during formation of a product (B) results in an observed slope in three-isotope space for A that is distinct from the intrinsic slope of the instantaneous fractionation process (Fig. S3A). In this study, the evolution of the reactant reservoir corresponds to the generation of an isotopically light Fe^{2+} pool through the removal of an isotopically heavy Fe^{3+} oxide product. The evolution of the reactant, written in δ’ notation, is

$$\delta'^{x}\mathrm{Fe}_A = (^{x}\alpha - 1)\times\ln\left(^{54}f_A\right)\times 1000 + \delta'^{x}\mathrm{Fe}_{A,i},$$

where $\delta'^{x}\mathrm{Fe}_{A,i}$ is the initial isotopic composition of the reactant, $\delta'^{x}\mathrm{Fe}_A$ is the isotopic composition of the reactant when a fraction $^{54}f_A$ of the reactant A remains, and $^{x}\alpha$ is the isotopic fractionation factor for isotope x in the reaction of A to form product B. In three isotope space, the isotopic composition of the reactant will evolve with an effective slope, $\theta^{56/57}_{\mathrm{eff}}$

$$\theta^{56/57}_{\mathrm{eff}} = \frac{\delta'^{56}\mathrm{Fe}_A - \delta'^{56}\mathrm{Fe}_{A,i}}{\delta'^{57}\mathrm{Fe}_A - \delta'^{57}\mathrm{Fe}_{A,i}} = \frac{\left(^{56}\alpha - 1\right)\times\ln\left(^{54}f_A\right)}{\left(^{57}\alpha - 1\right)\times\ln\left(^{54}f_A\right)} = \frac{^{57}\alpha^{\,\theta^{56/57}_{\mathrm{inst}}} - 1}{^{57}\alpha - 1},$$

where $\theta^{56/57}_{\mathrm{inst}}$ is the intrinsic slope for the instantaneous reaction. The distinctions between θ_{inst} and θ_{eff} are significant in the O and S isotope systems, where fractionations and relative isotopic mass differences are large. In the case of Fe isotopes, specifically Rayleigh distillation of

aqueous Fe^{2+} driven by oxidation and removal of Fe^{3+} minerals, the relevant values for $\theta^{56/57}_{inst}$ and $^{57}\alpha$ are 0.678 and on the order of 1.0015 respectively (*14*). Inserting these values results in $\theta^{56/57}_{eff} \approx 0.6778$, which is smaller than the intrinsic slope by only 0.0002 and not resolvable from the intrinsic slope for any naturally occurring range of fractionations (Fig. S3A). Nie *et al.* (*22*) provided a slightly different relation between the effective and intrinsic slopes for UV photo-oxidation, with $^{56}\alpha = 1.0012$, and determined the same result, that the effective slope for the evolving reactant reservoir was smaller than the instantaneous slope by just 0.0002 and thus the two slopes were indistinguishable within current measurement uncertainties. These calculations imply that discussing theoretical, single-step MFLs is an appropriate approximation for the evolution in triple Fe isotope space of an Fe^{2+} reservoir affected by oxidation and removal of Fe^{3+} products.

Mixing

Unlike fractionation processes, mixing lines are non-linear in logarithmic coordinates for isotopic ratios (Fig. S3B), so another pertinent question for this study is the degree to which $\epsilon'^{56}Fe$ *vs.* $\delta'^{57}Fe$ data may be explained by mixing systematics rather than distinct intrinsic MFLs. We define two isotopic reservoirs A and B as endmembers in a mixing array, and for the sake of simplicity (though this is not required), describe the linear tie-line between these two points as an instantaneous mass fractionation with the intrinsic slope and fractionation factors $\theta^{56/57}_{inst}$ and $\alpha_{A/B}$, respectively. Following Ono *et al.* (*53*) the magnitude of the effect of mixing on $\epsilon'^{56}Fe$ values is given as

$$\epsilon'^{56}Fe_{mix} - \epsilon'^{56}Fe_{MFL} = \left[\ln\left({}^{54}f_A\left({}^{57}\alpha_{A/B}{}^{\theta^{56/57}_{inst}} - 1\right) + 1\right) - \theta^{56/57}_{inst} \times \ln\left({}^{54}f_A\left({}^{57}\alpha_{A/B} - 1\right) + 1\right)\right] \times 10{,}000,$$

where $\epsilon'^{56}Fe_{mix}$ and $\epsilon'^{56}Fe_{MFL}$ refer to the points on the mixing curve and the MFL connecting A and B, respectively, and $^{54}f_A$ is the fraction of ^{54}Fe from A in the mixture. For $\epsilon'^{56}Fe$ *vs.* $\delta'^{57}Fe$ coordinates, this mixing curve is concave upward (Fig. S3B), analogous to the familiar example of $\Delta^{33}S$ *vs.* $\delta^{34}S$. When the most highly fractionated value in the Archean dataset, $\delta'^{57}Fe \approx -5$ ‰, is used as the endmember mixing with another endmember at $\delta'^{57}Fe = 0$ ‰, the maximum difference between $\epsilon'^{56}Fe_{mix}$ and $\epsilon'^{56}Fe_{MFL}$ is 0.0069 (Fig. S3B), which is an order of magnitude smaller than typical analytical precision for measurement of these values and hence they are unresolvable. Therefore, while mixing lines in these coordinates are not strictly linear, in practice they are very well approximated by straight lines and our data cannot be explained through non-linear mixing of endmembers lying on a single MFL.

Iron isotope MFLs

Mass-dependent triple-Fe-isotopic systematics have been explored in few publications to date, and only once previously in the context of low temperature aqueous geochemistry. Nie *et al.* (*22*) determined $\theta^{56/57} = 0.6785 \pm 0.0009$ associated with UV photo-oxidation of dissolved Fe^{2+} in anoxic solutions at near-neutral pH. A high precision measurement of the ca. 3.83 Ga IF-G geostandard from an IF in Isua, Greenland has $\epsilon'^{56}Fe$ and $\delta'^{57}Fe$ consistent with isotopically heavy ferric precipitates from those experiments (*22*) and both are within error of the high-temperature limit equilibrium law with $\theta^{56/57} = 0.678$. However, the magnitude of isotopic enrichment in IF-G and isotopically heavy IF oxides in general provide insufficient leverage in three-isotope space to distinguish different MFLs at the available precision for $\epsilon'^{56}Fe$. Whether different iron oxidation pathways for IF formation do have distinct MFLs has not yet been tested experimentally. However,

the fact that the high temperature equilibrium law, the MFL for photo-oxidation, and our observed MFL defined by IFs including Hotazel Mn-IF samples, which were most likely fractionated by direct O_2 oxidation (*25*), are all within error of one another suggests that fractionations of Fe isotopes driven by Fe^{2+}-Fe^{2+} equilibration may follow the equilibrium MFL regardless of the oxidation process involved. It will be important for future studies to constrain the value of $\theta^{56/57}$ for the remaining proposed oxidation pathway for IF, anoxygenic photoferrotrophy (*56*, *57*), however our results to date suggest it is unlikely that triple Fe isotopic systematics will be able to identify the oxidation pathway for IF due to the tendency of Fe^{2+} and Fe^{3+} to rapidly isotopically equilibrate.

Precipitation of pyrite is a kinetically controlled process associated with a large kinetic isotope effect (KIE) that enriches early precipitates in the light isotopes of Fe (*14*, *15*). The slope $\theta^{56/57}$ is anticipated to be shallower than that of equilibrium isotope fractionation (*19*, *20*), an expectation borne out in triple Fe isotopic measurements of olivine phenocrysts affected by iron diffusion (*21*). However, the value of $\theta^{56/57}$ relevant to pyrite precipitation did not have an empirical constraint prior to our study. Our pyrite precipitation experiments resulted in maximum DOP of ~14% (Fig. S2). By mass balance most iron was always left in the FeS_m pool and large fractionations from the starting composition of the experiment were observed in the pyrite pool, which provides leverage to determine the slope of the instantaneous MFL associated with pyrite precipitation. Our triple Fe isotopic analysis was consistent with a single kinetic MFL, with a slope of 0.0233 ± 0.0057 in ϵ'^{56}Fe *vs.* δ'^{57}Fe space, which translates to a slope $\theta^{56/57}_{KIE} = 0.6743 \pm 0.0006$. This is much shallower slope than that of the equilibrium limit law associated with redox equilibrium, but steeper than the exponential kinetic law that describes pure atomic transport (*19*, *20*).

Figures

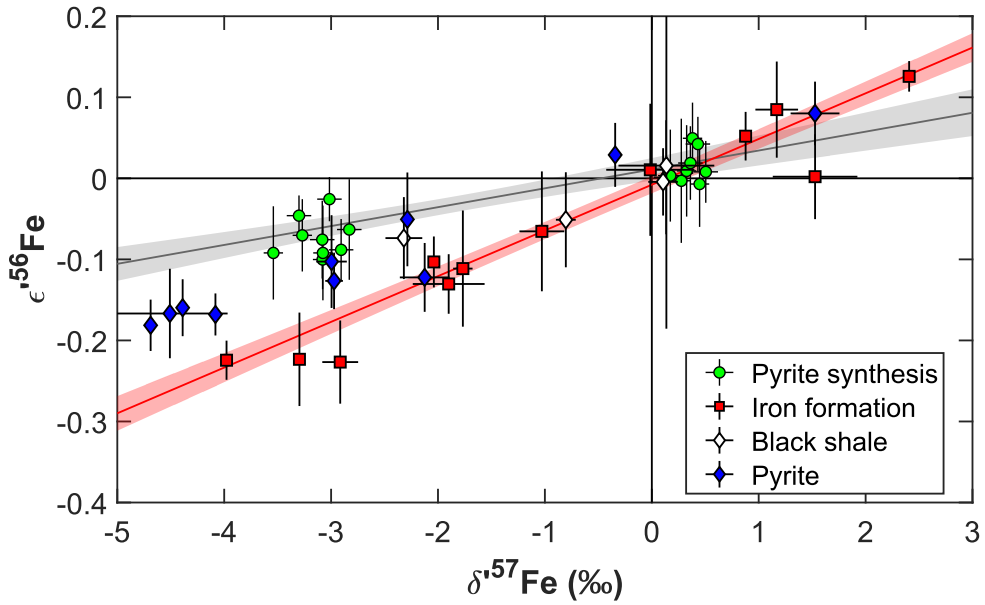

Fig. S1.
Triple-Fe-isotope systematics for IFs, pyrites, and black shales in ϵ'^{56}Fe *vs.* δ'^{57}Fe space, normalized to the exponential law. Error bars and envelopes are 95% confidence intervals. The slopes of endmember MFLs associated with iron-redox processes, and KIEs during pyritization, are constrained through analysis of isotopically light Mn-rich IFs and laboratory pyrite precipitation via the H_2S pathway (*14*, *24*, *35*), respectively. The slope of the IF MFL agrees with the theoretical equilibrium law, implying control by Fe^{2+}-Fe^{3+} equilibrium (*20*, *22*). Pyrite synthesis defines a kinetic MFL for pyrite precipitation. Pre-GOE pyrites fall in an intermediate space between redox equilibrium and kinetic endmembers.

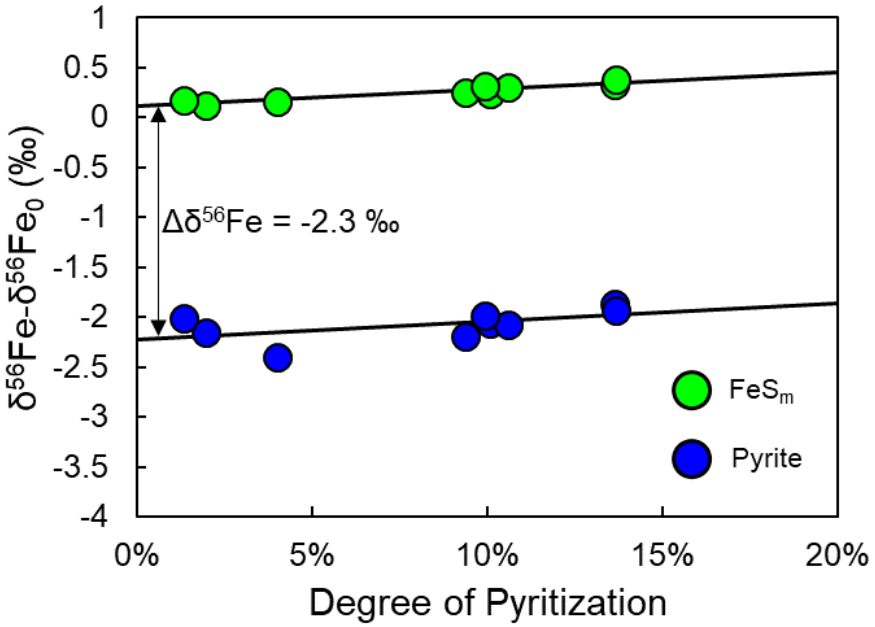

Fig. S2.

Iron isotopic fractionation between FeS_m and pyrite during abiotic precipitation of pyrite. The average Fe isotopic fractionation between FeS_m and pyrite, a shift in $\delta'^{56}Fe$ of -2.3 ‰, is determined both through taking the average difference between the two phases in individual experiments, and through the distance between linear fits of $\delta^{56}Fe$ vs. degree of pyritization. Low degrees of pyritization resulted in limited distillation of the reactant FeS_m reservoir poorly suited to determining a fractionation factor assuming Rayleigh distillation.

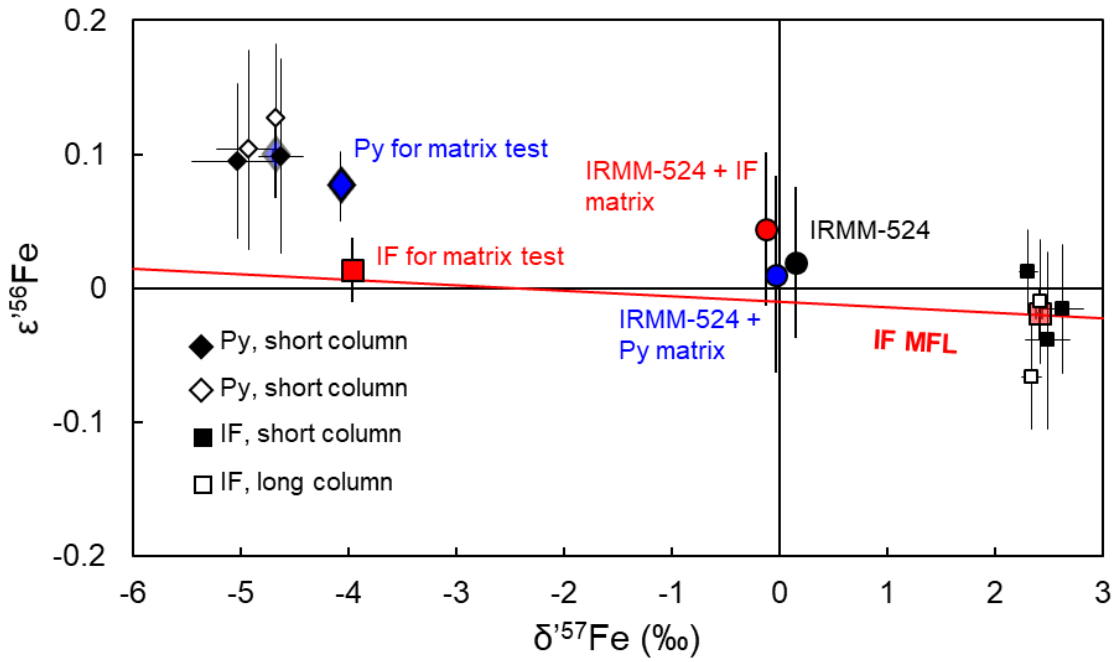

Fig. S3.

Tests performed on triple Fe isotopic analyses. Purification and analysis of replicate aliquots of IF sample JD-C 165A and pyrite sample SF-1 599.8 Py performed using short column (black filled symbols) and long column (open symbols) chromatography procedures, with average values for each sample shown in the pale colored symbols in the background. Despite some analytical scatter, we see no significant or systematic effect of using one purification procedure over another, and all replicate pyrite analyses were distinct from the triple Fe isotopic composition one would expect for a sample that was fractionated solely by the redox processes driving the IF MFL. Matrix mixing tests performed with IRMM-524 and matrix from IF sample REX 187.5 (bold red square) and pyrite sample SF-1 623.6 Py (bold blue diamond) revealed no resolvable matrix effect on ϵ'^{56}Fe analysis, with the pure IRMM-524 solution (black circle), IF matrix IRMM-524 solution (red circle), and pyrite matrix IRMM-524 solution (blue circle) all having ϵ'^{56}Fe values which are within error of one another and zero. Note that if matrix effects drove the difference between pyrite and IF triple Fe isotope variations, the IRMM-524 sample doped with pyrite matrix would need to have significantly more positive ϵ'^{56}Fe than the IF-doped standard, and it does not.

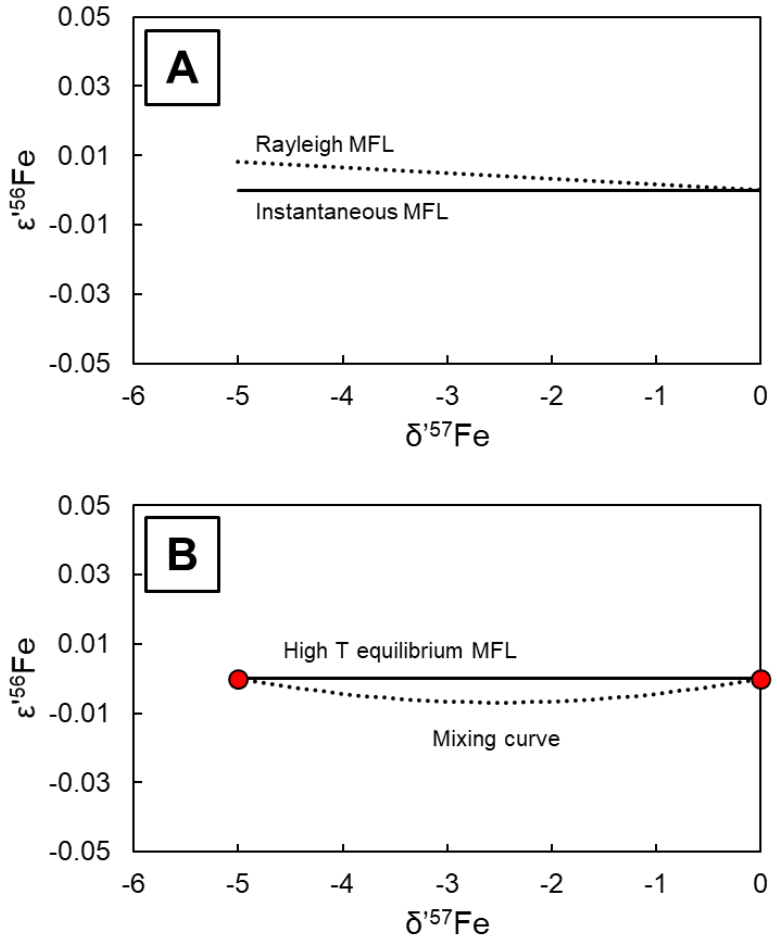

Fig. S4.

Distillation and mixing effects in triple Fe isotopic space. A: Comparison of effective MFL for Rayleigh distillation (dotted line) with the instantaneous MFL for the fractionation between reactant and product (solid line). The slopes equate to a difference in $\theta^{56/57}$ of just 0.0002, well within achievable analytical error for natural ranges of fractionation. B: Comparison of mixing curve (dotted line) between two arbitrary points (red circles) on the high-T equilibrium MFL (which is similar to our measured IF MFL), with the MFL itself (solid line). The maximum difference between the lines is 0.0069 in ϵ'^{56}Fe, much smaller than the achievable analytical error. Panels A and B indicate that distillation and mixing trends are identical to the instantaneous MFL of the process driving Fe isotopic fractionation over the naturally observed range of values, within analytical error on ϵ'^{56}Fe, which is typically on the order of ±0.05 (95 % C.I.).

892

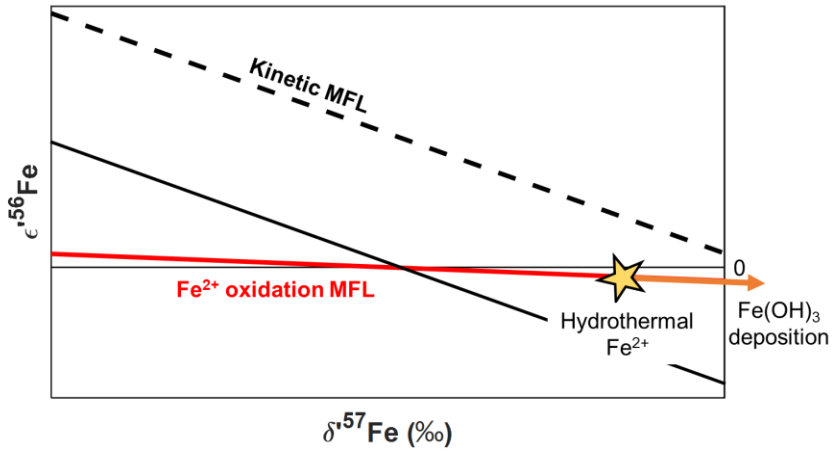
Kinetic MFL
ϵ'^{56}Fe
Fe^{2+} oxidation MFL
0
$Fe(OH)_3$ deposition
Hydrothermal Fe^{2+}
δ'^{57}Fe (‰)

893

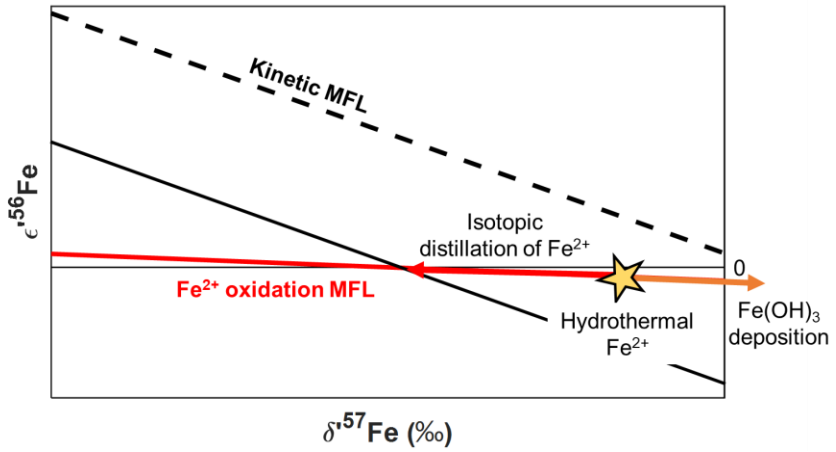
Kinetic MFL
ϵ'^{56}Fe
Isotopic distillation of Fe^{2+}
Fe^{2+} oxidation MFL
0
$Fe(OH)_3$ deposition
Hydrothermal Fe^{2+}
δ'^{57}Fe (‰)

894

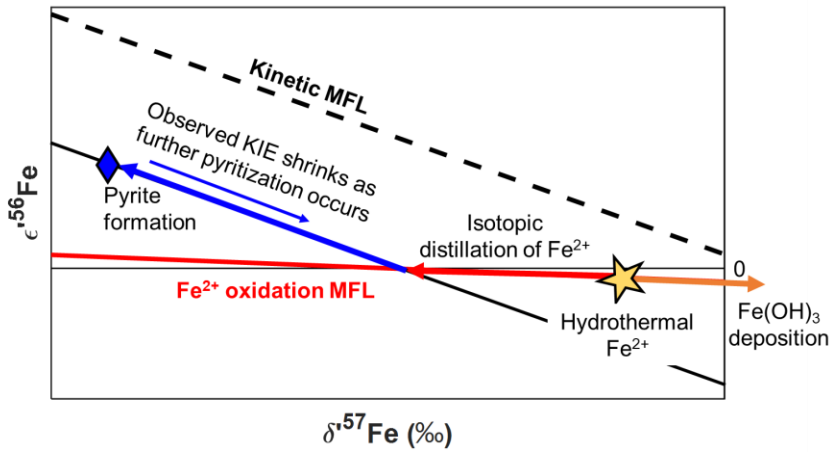
Kinetic MFL
Observed KIE shrinks as further pyritization occurs
ϵ'^{56}Fe
Pyrite formation
Isotopic distillation of Fe^{2+}
Fe^{2+} oxidation MFL
0
$Fe(OH)_3$ deposition
Hydrothermal Fe^{2+}
δ'^{57}Fe (‰)

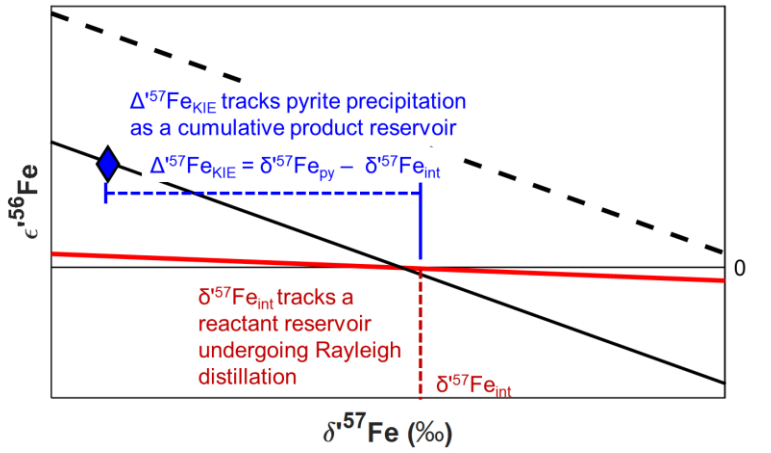

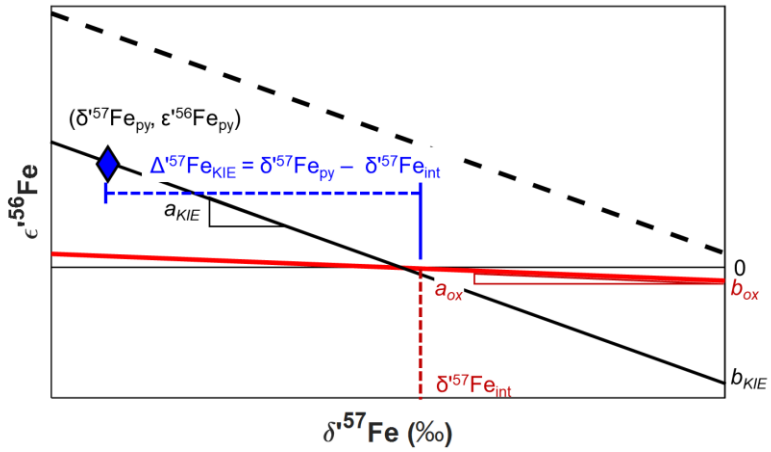

Fig. S5.

Conceptual illustration of the two step process (Fe^{2+} isotopic distillation by partial oxidation; subsequent partial pyritization) we propose for generating triple-Fe-isotopic composition of isotopically depleted pre-GOE pyrites, and the procedure for determining Fe isotopic contributions of pyritization, and initial isotopic composition of the pyrite-forming water mass, to the Fe isotopic composition of pyrite. The $\delta'^{57}Fe$ value at where a trajectory for KIE during pyrite precipitation (with slope a_{KIE}) intercepts the oxidative IF MFL ($\delta'^{57}Fe_{int}$) is determined by solving of simultaneous line equations. The difference between $\delta'^{57}Fe_{int}$ and $\delta'^{57}Fe_{py}$ gives the expression of the KIE during pyritization, which is used to determine the degree of pyritization (f_{py}) of the pre-pyritization water mass assuming that the pyrite is a cumulative product of all precipitated pyrite. $\delta'^{57}Fe_{int}$ is assumed to be the $\delta'^{57}Fe$ value of the pre-pyritization water mass, and its isotopic composition is assumed to reflect the degree of isotopically heavy Fe^{3+}-(oxyhydr)oxide removal (F_{ox}) that took place prior to the formation of pyrite.

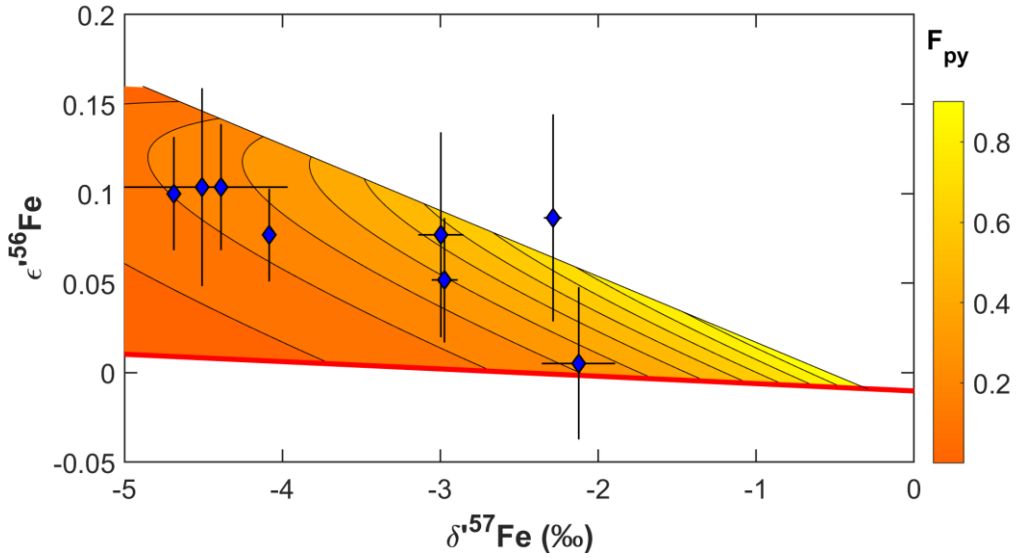

Fig. S6.

Determining the fractional pyrite sink for upwelled Fe (F_{py}) from triple-Fe-isotopic data. F_{py} values are calculated as $F_{py} = f_{py} \times (1 - F_{ox})$. Corresponding f_{py} and F_{ox} contours are plotted in Figure 2B of the main text.

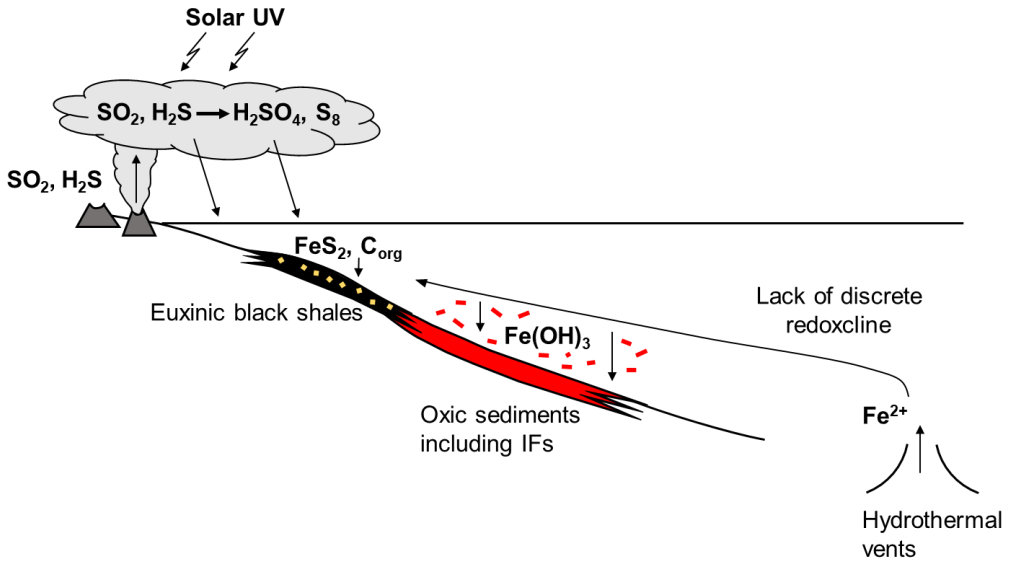

Fig. S7.

Basin cross-section illustrating marine iron cycle before the GOE informed by triple-Fe-isotope systematics (*9*, *10*, *27*)**.** Dissolved Fe^{2+} in deep-ocean waters fed by hydrothermal vents was upwelled onto continental margins. Oxidation of Fe^{2+} across a spatially diffuse redoxcline led to deposition of Fe^{3+}-(oxyhydr)oxide-rich sediments including IFs. In sedimentary environments with high organic carbon burial, the remaining dissolved Fe^{2+} was incorporated into pyrite, with pyritization before the GOE being limited by sulfur availability under a volcanically- and atmospherically-influenced sulfur cycle (*3*, *58*).

Table S1

Triple Fe isotope data for Archean-Paleoproterozoic pyrites, black shales, and IFs

Sample	Age (Ga)	Sample type	$\delta'^{56}Fe$	2 s.e	$\delta'^{57}Fe$	2 s.e	$\epsilon'^{56}Fe_{exp}$	$\epsilon'^{56}Fe_{eq}$	2 s.e	n
EBA-1 1057.5 Py	2.32	pyrite	1.034	0.153	1.527	0.229	0.080	-0.012	0.039	42
EBA 2/30 Py	2.32	pyrite	-2.023	0.095	-2.996	0.143	-0.103	0.077	0.057	12
DO29 14.95 Py	2.5	pyrite	-1.539	0.037	-2.286	0.057	-0.051	0.087	0.058	34
WB-98 520.8 Py	2.52	pyrite	-2.010	0.056	-2.972	0.083	-0.127	0.052	0.035	33
WB-98 519.68 Py	2.52	pyrite	-1.440	0.156	-2.125	0.232	-0.122	0.005	0.042	27
SF-1 599.88 Py	2.65	pyrite	-3.166	0.018	-4.688	0.025	-0.181	0.100	0.032	53
SF-1 623.6 Py	2.65	pyrite	-2.762	0.020	-4.082	0.028	-0.168	0.077	0.026	76
SF-1 642.8 Py	2.65	pyrite	-0.228	0.024	-0.343	0.035	0.029	0.049	0.039	55
FVG-1 752.8 A Py	2.66	pyrite	-3.046	0.367	-4.508	0.540	-0.167	0.104	0.055	21
FVG-1 752.8 B Py	2.66	pyrite	-2.967	0.020	-4.389	0.030	-0.160	0.104	0.035	55
EBA-1 1057.5 BS	2.32	black shale	0.072	0.091	0.105	0.139	-0.004	-0.011	0.042	46
FVG-1 765.8 BS	2.66	black shale	-0.546	0.064	-0.804	0.093	-0.051	0.065	0.059	12
FVG-1 774 BS	2.66	black shale	-1.577	0.123	-2.319	0.172	-0.074	0.008	0.051	29
FVG-1 827.8 BS	2.66	black shale	0.093	0.284	0.136	0.448	0.016	-0.003	0.201	10
REX 167.5	2.40	IF	-1.981	0.115	-2.915	0.168	-0.227	0.014	0.051	12
REX 187.5	2.40	IF	-2.692	0.008	-3.978	0.011	-0.224	-0.052	0.024	109
Hotazel #41	2.40	IF	-2.237	0.034	-3.296	0.044	-0.223	-0.026	0.058	22
RM5	2.47	IF	-0.008	0.276	-0.014	0.412	0.011	0.011	0.082	12
WIT-18-740A	2.48	IF	-1.199	0.067	-1.767	0.090	-0.111	-0.005	0.072	10
ZO4-31	2.70	IF	0.796	0.132	1.169	0.200	0.085	0.015	0.059	26
JD-C165A	2.74	IF	1.624	0.019	2.407	0.028	0.126	-0.019	0.019	184
JD-65-296-1	2.74	IF	1.030	0.265	1.527	0.396	0.002	-0.090	0.052	23
PO5-1	2.95	IF	-1.384	0.028	-2.039	0.039	-0.103	-0.016	0.031	55
PO5-6	2.95	IF	-0.696	0.142	-1.028	0.210	-0.065	0.019	0.074	26
PO5-7	2.95	IF	-1.290	0.224	-1.900	0.336	-0.130	-0.004	0.037	12
IF-G	3.83	IF	0.611	0.012	0.878	0.019	0.052	-0.001	0.030	24

All isotope ratios are reported normalized to IRMM-014. The value of n refers to the number of standard-sample brackets analyzed.

Table S2

Triple Fe isotopic data for pyrite precipitation experiments

Sample	$\delta'^{56}Fe-\delta'^{56}Fe_0$	2 s.e.	$\delta'^{57}Fe-\delta'^{57}Fe_0$	2 s.e.	n(δ)	$\epsilon'^{56}Fe_{exp}-\epsilon'^{56}Fe_{exp,0}$	$\epsilon'^{56}Fe_{eq}-\epsilon'^{56}Fe_{eq,0}$	2 s.e.	n(ϵ)
SB1 FeS	0.243	0.064	0.381	0.091	5	0.049	0.027	0.044	21
SB1 Py	-2.201	0.064	-3.269	0.091	5	-0.070	0.126	0.045	26
SB2 FeS	0.159	0.064	0.276	0.091	5	-0.003	-0.020	0.077	10
SB2 Py	-2.582	0.064	-3.540	0.091	5	-0.092	0.120	0.058	9
SB3 FeS	0.232	0.064	0.326	0.091	5	0.009	-0.010	0.056	20
SB3 Py	-2.072	0.064	-3.080	0.091	5	-0.100	0.085	0.037	17
SB4 FeS	0.302	0.064	0.447	0.091	5	-0.007	-0.034	0.053	9
SB4 Py	-2.078	0.064	-3.077	0.091	5	-0.092	0.093	0.058	10
SB5 FeS	-0.026	0.061	0.133	0.115	5	0.001	-0.007	0.070	9
SB5 Py	0.091	0.061	-3.300	0.115	5	-0.046	0.152	0.025	27
SB6 FeS	-2.177	0.061	0.173	0.115	5	0.003	-0.007	0.057	9
SB6 Py	0.150	0.061	-3.083	0.115	5	-0.076	0.109	0.048	9
SB8 FeS	-2.039	0.061	0.361	0.115	5	0.019	-0.003	0.045	20
SB8 Py	0.289	0.061	-3.016	0.115	5	-0.026	0.155	0.027	28
SB9 FeS	-2.017	0.061	0.431	0.115	5	0.042	0.016	0.034	27
SB9 Py	0.301	0.061	-2.830	0.115	5	-0.063	0.107	0.062	20
SB10 FeS	-1.899	0.061	0.505	0.115	5	0.008	-0.022	0.038	29
SB10 Py	0.358	0.061	-2.906	0.115	5	-0.088	0.086	0.038	28

All isotope ratios are reported normalized to the composition of the starting material for experiments. The values of n(δ) and n(ϵ) refer to the number of standard-sample brackets analyzed for δ and ϵ measurements respectively. Starting material for SB 1-4, and SB 5-10, were analyzed 40, and 76 times, respectively.

Table S3

Geological unit and age information for Archean-Paleoproterozoic pyrite, black shales, and IFs

Sample	Geological unit	Age (Ga)	Sample type	Refs.
EBA-1 1057.5 Py	Timeball Hill Fm	2.32	pyrite	(*9*)
EBA 2/30 Py	Timeball Hill Fm	2.32	pyrite	(*9*)
DO29 14.95 Py	Mount McRae Shale	2.50	pyrite	(*9*)
WB-98 520.8 Py	Gamohaan Fm	2.52	pyrite	(*9*)
WB-98 519.68 Py	Gamohaan Fm	2.52	pyrite	(*9*)
SF-1 599.88 Py	Lokammona Fm	2.65	pyrite	(*9*)
SF-1 623.6 Py	Lokammona Fm	2.65	pyrite	(*9*)
SF-1 642.8 Py	Lokammona Fm	2.65	pyrite	(*9*)
FVG-1 752.8 A Py	Jeerinah Fm	2.66	pyrite	(*9*)
FVG-1 752.8 B Py	Jeerinah Fm	2.66	pyrite	(*9*)
EBA-1 1057.5 BS	Timeball Hill Fm	2.32	black shale	(*9*, *26*)
FVG-1 765.8 BS	Jeerinah Fm	2.66	black shale	(*9*, *26*)
FVG-1 774 BS	Jeerinah Fm	2.66	black shale	(*9*, *26*)
FVG-1 827.8 BS	Jeerinah Fm	2.66	black shale	(*9*, *26*)
REX 167.5	Hotazel Fm	2.43	IF	(*2*, *25*, *45*)
REX 187.5	Hotazel Fm	2.43	IF	(*2*, *25*, *45*)
Hotazel #41	Hotazel Fm	2.43	IF	(*2*, *25*, *45*)
RM5	Brockman IF	2.47	IF	(*10*)
WIT-18-740A	Westerburg area IF	2.48	IF	(*10*)
ZO4-31	Manjeri IF	2.70	IF	(*10*)
JD-C165A	Mary River IF	2.74	IF	(*10*)
JD-65-296-1	Mary River IF	2.74	IF	(*10*)
PO5-1	Mozaan Gp	2.95	IF	(*10*)
PO5-6	Mozaan Gp	2.95	IF	(*10*)
PO5-7	Mozaan Gp	2.95	IF	(*10*)
IF-G	Isua Supracrustal Belt	3.83	IF	(*44*, *46*)

Reference numbers refer to Supplementary Reference List in the Supplementary Information

Table S4

Estimated fractional size of iron sinks and shelf sedimentary Fe/S ratios for isotopically light pyrites

Sample	F_{ox}	F_{py}	F_{sulf}	$(Fe/S)_{sed}$	Moles O_2 yield (per mole FeS_2)
EBA 2/30	$0.38^{+0.45}_{-0.36}$	$0.68^{+0.30}_{-0.47}$	$0.48^{+0.14}_{-0.21}$	$0.9^{+2.0}_{-0.4}$	$2.3^{+0.2}_{-1.0}$
DO29 14.95	$0.22^{+0.51}_{-0.21}$	$0.60^{+0.32}_{-0.47}$	$0.65^{+0.12}_{-0.38}$	$0.7^{+1.2}_{-0.2}$	$2.4^{+0.1}_{-0.6}$
WB-98 520.8	$0.52^{+0.28}_{-0.44}$	$0.83^{+0.15}_{-0.26}$	$0.40^{+0.21}_{-0.20}$	$1.1^{+1.4}_{-0.5}$	$2.2^{+0.3}_{-0.7}$
WB-98 519.68	$0.64^{+0.24}_{-0.47}$	$0.98^{+0.02}_{-0.15}$	$0.36^{+0.34}_{-0.23}$	$1.4^{+2.6}_{-0.8}$	$2.1^{+0.3}_{-1.3}$
SF-1 599.88	$0.64^{+0.32}_{-0.46}$	$0.58^{+0.28}_{-0.41}$	$0.20^{+0.02}_{-0.08}$	$2.0^{+2.1}_{-1.0}$	$1.7^{+0.5}_{-1.0}$
SF-1 623.6	$0.50^{+0.31}_{-0.43}$	$0.58^{+0.29}_{-0.42}$	$0.30^{+0.03}_{-0.14}$	$1.3^{+1.7}_{-0.7}$	$2.1^{+0.3}_{-0.8}$
FVG-1 752.8 A	$0.57^{+0.32}_{-0.49}$	$0.54^{+0.37}_{-0.45}$	$0.23^{+0.02}_{-0.13}$	$1.7^{+3.4}_{-1.0}$	$1.9^{+0.5}_{-1.7}$
FVG-1 752.8 B	$0.52^{+0.30}_{-0.46}$	$0.54^{+0.30}_{-0.40}$	$0.25^{+0.02}_{-0.10}$	$1.5^{+1.6}_{-0.9}$	$2.0^{+0.4}_{-0.8}$

Uncertainties are 95 % confidence intervals from Monte Carlo simulations. O_2 yields assume volcanic H_2S/SO_2 input ratio of 0. For volcanic H_2S/SO_2 input ratio of 1, O_2 yields are smaller by a factor of 2.5